

# Optoelectronic Neural Implant Sensors for Cerebral Blood Volume Monitoring

Christopher Choi

Submitted in partial fulfillment of the  
requirements for the degree  
of Doctor of Philosophy  
in the Graduate School of Arts and Sciences

**COLUMBIA UNIVERSITY**

2018

©2018

Christopher Choi

All Rights Reserved

## **Abstract**

# **Optoelectronic Neural Implants for Cerebral Blood Volume Monitoring**

**Christopher Choi**

Nearly 50 million people are afflicted with epilepsy, worldwide. These patients suffer from unprovoked seizures, where neurons in the cerebral cortex undergo uncontrolled, hypersynchronous firing of neurons. 30% of patients with epilepsy do not respond to drug treatments. For these patients, surgical treatment involving the removal or disconnection of brain matter is one of the only alternatives. Such surgical treatments often rely on long-term monitoring of neuronal activity in the brain using subdurally implanted surface electrodes to locate the epileptic focus, but these clinical methods for mapping neuronal activity suffer from low spatial resolutions and poor noise, which can limit the success of surgical treatments where an error of even 1 mm can be critical.

The work described here involves the development of an implantable system for performing optical recordings of intrinsic signal (ORIS) on the surface of the brain. By taking advantage of the unique absorption spectrum of hemoglobin, cerebral blood volume (CBV) can be measured via reflectivity changes in the brain at specific wavelengths of light. Due to the metabolic demands of the brain, the exaggerated neuronal activity and spiking associated with epileptic seizures can be detected indirectly through changes in CBV. While high resolution ORIS measurements have been recorded using externally mounted CCD sensors, this work presents some of the first developments in producing a fully implantable ORIS sensor.

Progress in the development of an implantable ORIS sensor described here includes: an implantable organic light emitting diode (OLED) and organic photodetector (OPD) integrated on a highly flexible parylene-c substrate, an implantable sensor using a microLED array embedded on a flexible polyimide substrate, and the application of quantum dots to microLEDs for optical down-conversion. Successful in vivo detection of seizures is achieved with high signal-to-noise using these methods. Additionally, spatial localization of seizure

activity is performed using the microLED array. These developments represent crucial first steps in the development of a full 2D neuronal mapping system using implantable ORIS devices.



# Contents

<b>List of Figures</b>	<b>iii</b>
<b>List of Tables</b>	<b>x</b>
<b>1 Introduction</b>	<b>1</b>
1.1 Epileptic Seizures . . . . .	1
1.1.1 Seizure Propagation and Treatment . . . . .	3
1.1.2 Mapping Neural Activity . . . . .	4
1.2 High Resolution Imaging . . . . .	5
1.3 Optical Recording of Intrinsic Signal (ORIS) . . . . .	6
1.4 Objectives and Approach . . . . .	7
<b>2 Basics of Flexible Optoelectronics</b>	<b>9</b>
2.1 Introduction . . . . .	9
2.2 LEDs and Photodiodes . . . . .	9
2.3 Organic Semiconductors . . . . .	12
2.3.1 Organic LED (OLED) . . . . .	14
2.3.2 Organic Photodetector (OPD) . . . . .	17
2.3.3 Fabrication Methods . . . . .	19
2.3.4 Biomedical Applications for OLED and OPD . . . . .	20
2.4 MicroLED . . . . .	24
2.5 Colloidal Quantum Dots . . . . .	29
2.5.1 Electroluminescent QDLEDs vs. Photoluminescent QDs . . . . .	29
2.5.2 Biomedical Applications for Quantum Dots . . . . .	30

<b>3</b>	<b>Integrated Organic LED and Organic Photodetector on a Highly Flexible Parylene-C Substrate</b>	<b>36</b>
3.1	Highly flexible substrate . . . . .	36
3.2	OLED and OPD Structure . . . . .	37
3.3	Fabrication . . . . .	39
3.4	Device Performance . . . . .	40
3.5	<i>In Vivo</i> Measurement of Neural Activity and Detection of Seizures . . . . .	44
3.6	Chapter Summary . . . . .	48
<b>4</b>	<b>MicroLED Based Sensor</b>	<b>49</b>
4.1	Bi-directional Emitter/Detector MicroLEDs . . . . .	49
4.2	Device Fabrication . . . . .	51
4.3	In-Vivo Measurement of CBV and Seizure Detection . . . . .	53
4.4	MicroLED ORIS Sensor with Quantum Dot Optical Down-Conversion Coating	58
4.5	Chapter Summary . . . . .	62
<b>5</b>	<b>Conclusion</b>	<b>63</b>
	<b>Bibliography</b>	<b>66</b>
	<b>Appendix</b>	<b>78</b>

# List of Figures

1.1	Diagram of the cerebral hemispheres.[16] Image courtesy of blausen.com staff (2014). "Medical gallery of Blausen Medical 2014". WikiJournal of Medicine 1 (2). DOI:10.15347/wjm/2014.010. ISSN 2002-4436. Reused under the Creative Commons Attribution 3.0 Unported license <a href="https://goo.gl/KfFFfo">https://goo.gl/KfFFfo</a>	2
1.2	Schematic diagram of ECoG measurement using a subdurally implanted array of surface electrodes.[16] Standard clinical surface electrodes can perform chronic measurement of neural activity, but have relatively low spatial resolutions ( $< 1$ cm). Image courtesy of: Blausen.com staff (2014). "Medical gallery of Blausen Medical 2014". WikiJournal of Medicine 1 (2). DOI:10.15347/wjm/2014.010. ISSN 2002-4436. Reused under the Creative Commons Attribution 3.0 Unported (CC BY 3.0) license <a href="https://goo.gl/KfFFfo">https://goo.gl/KfFFfo</a>	5
1.3	Hemoglobin absorbance spectra. Measuring reflectivity of light at isosbestic wavelengths where oxygenated and deoxygenated hemoglobin absorb light equally gives a relative measure of total CBV. The devices in this work target the isosbestic points at 449 nm, 522 nm, and 548 nm. Absorbance data provided by Prahl, et al.[30]	7
2.1	Schematic showing the design and operation of an implantable ORIS sensor. The primary elements include an LED and a photodetector integrated on a thin, highly flexible substrate.	10
2.2	Schematic diagram of an LED. Radiative recombination in the p-n junction results in light emission at photon energies equal to the bandgap.	11

2.3	Schematic diagram of a photodiode. Incident light on the photodiode creates charge separation due to the photoelectric effect. The charges are swept towards the contacts due to the intrinsic electric field, generating a photocurrent.	11
2.4	The resonance forms of naphthalene. The alternating double and single bonds form conjugate pairs, with the extra electrons forming the double bonds not having a specific localized orientation. This charge conjugation is the mechanism which gives rise to charge transport and semiconducting properties of organic semiconductors.	13
2.5	Example of the band structure of an OLED. Recombination in the EML results in green light emission whose wavelength is determined by the HOMO-LUMO gap of AlQ <sub>3</sub> .	14
2.6	Diagram of singlet and triplet excited states.	16
2.7	Photoexcitation and free charge conversion in a donor-acceptor junction.	18
2.8	a) Organic pulse oximeter replaces inorganic optoelectronic elements with OLEDs and OPDs (b) Hardware block diagram for the system including amplification and a microcontroller for data acquisition (c,d) Simultaneous oximetry measurements with a commercially available inorganic oximeter probe and the organic oximeter probe, respectively. Heart rate is determined from the timing of the systolic peaks in the oximetry signals. The ratio of transmitted light at two wavelengths was used to calculate blood oxygen saturation using Beer–Lambert’s law. [57] Reprinted by permission from Lochner, Claire M., et al. "All-organic optoelectronic sensor for pulse oximetry." <i>Nature communications</i> 5 (2014): 5745.	21
2.9	Miniaturized biosensor using OPDs. [58] a) A glass slide with a printed OPD sensor is used for CL detection of SEB b) The glass slide is placed into a portable controller for data acquisition. Reprinted with permission from Wojciechowski, Jason R., et al. "Organic photodiodes for biosensor miniaturization." <i>Analytical chemistry</i> 81.9 (2009): 3455-3461. Copyright 2009 American Chemical Society.	22

2.10	CL detection of SEB using an OPD. [58] Substrates treated with $\alpha$ -SEB, SEB, and $\alpha$ -SEB-HRP were added ~20 s into recording. The concentration of SEB detected measured in this plot was 5 ng/mL. Reprinted with permission from Wojciechowski, Jason R., et al. "Organic photodiodes for biosensor miniaturization." <i>Analytical chemistry</i> 81.9 (2009): 3455-3461. Copyright 2009 American Chemical Society.	24
2.11	Strain engineered flexible microLED display. [63] Reprinted by permission from Byun, Junghwan, et al. "Fully printable, strain-engineered electronic wrap for customizable soft electronics." <i>Scientific Reports</i> 7 (2017): 45328.	26
2.12	Wireless optogenetic stimulation of mice using a microLED implant a) A mouse implanted with the wireless blue microLED implant was confined to an enclosure containing a resonant cavity for wireless power delivery. The blue microLED was powered on wirelessly, triggering a circulatory motor behavior induced by the activation of Chr2 b) Schematic of the wireless microLED implant c) Photograph of the microLED implant [65] Reprinted by permission from Montgomery, Kate L., et al. "Wirelessly powered, fully internal optogenetics for brain, spinal and peripheral circuits in mice." <i>Nature methods</i> 12.10 (2015): 969-974.	28
2.13	Schematic diagram of QDs used in targeted photodynamic therapy for tumor suppression. [79] Reprinted from <i>Biomaterials</i> 34.4, Hsu, Chia-Yen, et al., "Bioluminescence resonance energy transfer using luciferase-immobilized quantum dots for self-illuminated photodynamic therapy.", Pages 1204-1212, Copyright 2013, with permission from Elsevier.	31

2.14	Tumor suppression via QD-enabled targeted photodynamic therapy.[79] a) Tumor volume was tracked for the different permutations of treatments. Mice which received the BRET-induced photodynamic therapy showed a reduction in tumor volume b) Stained sections of tumors c) Microscope image of tumors. Reprinted from Biomaterials 34.4, Hsu, Chia-Yen, et al., "Bioluminescence resonance energy transfer using luciferase-immobilized quantum dots for self-illuminated photodynamic therapy.", Pages 1204-1212, Copyright 2013, with permission from Elsevier. . . . .	32
2.15	QDLED structure and performance. [81] a) Inverted QDLED structure b) Emission spectrum of the EL QDLED. Insets show the structure of the QD and a photograph of a completed QDLED c) Electroluminescent performance of the QDLED reported d) The QDLED is a high efficiency device capable of high brightness. Reprinted by permission from Chen, Hao, et al. "Quantum dot light emitting devices for photomedical applications." Journal of the Society for Information Display 25.3 (2017): 177-184. . . . .	34
2.16	Photograph and schematic of the QDLED photobiomodulation therapy. [81] a) Photograph of the red QDLED with 620 nm peak emission b) The QDLED is placed underneath the transparent cell culture wells to perform in-vitro photobiomodulation therapy c) Schematic of the control experiment with no illumination d) Schematic of the cell lines receiving photobiomodulation therapy using a QDLED. Reprinted by permission from Chen, Hao, et al. "Quantum dot light emitting devices for photomedical applications." Journal of the Society for Information Display 25.3 (2017): 177-184. . . . .	35
3.1	Parylene-C Structure . . . . .	37
3.2	Schematic of the OLED and OPD structure. A photograph showing the layout of the OLED and OPD on the ORIS device is shown. . . . .	38
3.3	Fabrication of Organic Implantable ORIS Sensor . . . . .	40
3.4	Flexible ORIS Sensor . . . . .	41
3.5	OLED Emission Spectrum . The emission spectrum has a peak emission at 540 nm which overlaps with an isosbestic wavelength for hemoglobin. . . . .	42

3.6	Normalized Spectral Response of OPD . The 540nm isosbestic wavelength used in the ORIS measurements is denoted with a dashed line. . . . .	42
3.7	OPD Photocurrent Response. The ON/OFF ratio between photocurrent generated under illumination and the background current under dark conditions is over 1500 . . . . .	43
3.8	OLED Electrical Current and Light Output. With a bias voltage of 8.2 V, the OLED outputs 5.6 $\mu$ W of light, roughly 100 cd/m <sup>2</sup> . . . . .	43
3.9	OLED Operational Lifetime. The luminance half-life is marked with a dashed line. The device has a lifetime over an hour when exposed to saline solution. . . . .	44
3.10	Photo of the organic ORIS device attached to the surface of the brain. The OLED and OPD elements are circled in yellow, while the needle electrode is marked by a green box. . . . .	45
3.11	Baseline variations in the CBV of the animal's brain recorded by the organic ORIS device. The optical intrinsic (OI) signal captured by the organic ORIS device is shown at the top with a fast Fourier transform (FFT) of the OI shown directly below it. Isolated signals of SSHO, respiration, and heartbeat are extracted from the OI signal by notch filtering and plotted. . . . .	46
3.12	<i>In vivo</i> seizure detection using the organic ORIS device. The two plots at the top show the LFP and OI signal recorded simultaneously during a sequence of seizures. The duration of seizures is shaded in pink. A more detailed view of a single seizure that occurred in the middle of the sequence is shown below. The processed OI signal was produced by removing the oscillations due to heartbeat and respiration, a significant source of noise in detecting seizures. . . . .	47
4.1	Photograph of the microLEDs soldered onto a glass substrate with a Cr/Au circuit. DA1000 LED (left) is 1 mm in length. DA 850 (right) is 850 $\mu$ m in length. . . . .	49
4.2	Spectral response of the microLEDs . . . . .	50

4.3	Fabrication steps for the microLED ORIS sensor. a) 40 nm Cr and then 150 nm Au are thermally evaporated onto a 25 $\mu$ m thick, clean polyimide sheet on a glass carrier. b) The circuit and bond pads are patterned via photolithography and wet etching. c) Flux is applied to the bond pads and the microLEDs are placed on the bond pads. The microLEDs are reflowed in an infrared reflow oven at 280 C. d) PMMA resist is deposited over the bonded microLEDs using a pneumatic printer. The devices are annealed at 100 C for 90 minutes to harden the PMMA resist and remove the solvent. e) Parylene-C is blanket-coated over the entire device after contacting the devices hot bar bonding. f) The completed device is delaminated from the glass carrier. . . . .	52
4.4	Photographs of the ORIS devices in operation. Left: Completed ORIS device is shown with a blue microLED operating in emitter mode. Middle: ORIS device flexed around a rod with 1/2 inch diameter. A green microLED is shown operating at the same time. Right: MicroLED ORIS device attached to the surface of a rat's brain. . . . .	52
4.5	Baseline Measurements of CBV by the microLED ORIS device. Left: ORIS measurement of baseline CBV signals. Variations in the ORIS signal are due to changes in CBV. Right: FFT of the baseline CBV signals. . . . .	53
4.6	<i>In vivo</i> seizure detection using blue-to-green microLED ORIS device. Duration of seizures are shaded in pink. Seizures are detected with a signal-to-noise ratio greater than 33 dB. SNR is determined by comparing the root mean square amplitude of the baseline oscillations to the excursion in amplitude during seizure events. . . . .	54
4.7	<i>In vivo</i> seizure detection using blue-to-blue microLED ORIS device. Duration of seizures are shaded in pink. High SNR of seizure detection is achieved despite the lower responsivity of the blue microLEDs. . . . .	55
4.8	Layout of the linear array device. The two microLEDs in photodiode mode, PD1 and PD2, are attached roughly 2 mm and 3.2 mm away from the focus of the seizure which occurs at the site of 4AP injection. . . . .	57



4.9	Localized measurements of CBV using a linear array of microLEDs. The microLED detector labeled “PD2” is 1.2 mm further away from the focus of the seizure than PD1. The duration of seizures at the epileptic focus are highlighted in pink. Notch filtering to remove the out of band signals is used to improve the detection of seizures. . . . .	57
4.10	Pneumatic printing QD optical down-conversion coatings. Photographs left to right: pneumatic printing set up, green QD coating being applied to a microLED, microLED with applied amber QD coating. . . . .	59
4.11	Emission spectra for MicroLED coatings without filtering. The blue component of the emitted light is from microLED backlight that has not been absorbed or has been back-reflected from the substrate. . . . .	59
4.12	Emission spectra of optical QD down-conversion of blue microLED backlight. Inset: photographs of the microLEDs with QD coatings shown operating. Roscolux gel filters and polyimide sheets are used to filter any blue emission not absorbed by the QDs. . . . .	60
4.13	Seizure detection using a microLED ORIS device with green QD down-conversion coating. Duration of seizures is highlighted in pink. Notch filtering to remove the out-of-band signals is used to improve the detection of seizures. . . . .	61
5.1	Diagram of 3 variants of CdS/CdSe/CdS core shell quantum dots. . . . .	80
5.2	QD absorption (left) and photoluminescent (right) spectra for 3 different variants of CdS/CdSe/CdS core shell QDs suspended in toluene. . . . .	80

# List of Tables

4.1	Responsivity of microLEDs in photodiode mode to 3 different light emissions used in the ORIS device. . . . .	51
-----	-----------------------------------------------------------------------------------------------------------------	----

# Acknowledgements

I would like to acknowledge and thank my advisor, Professor Ioannis Kymissis, for his mentorship and guidance on this project, my education, and my career. His passion for technology and engineering innovation has inspired and driven me through my time at Columbia. I am grateful for all the opportunities, lessons, and patients that he has provided.

I would also like to acknowledge and thank Professor Hongtao Ma, who I worked closely with in completing this work.

I would like to acknowledge and thank Youngwan Kim, whose contributions, effort, time dedicated to this work cannot be overstated.

Thank you to my family for their unwavering support and love. To Mom, Dad, Andrew, Nathan, thank you for always believing in me. To my extended family, thank you for rooting for me all these years.

Thank you to my friends, in New York and beyond. Special thanks go out to Ting-Ting Zhou, E-dean Fung, and Wesley Chao for their aid in proofreading this document.

I would like to acknowledge the members of the committee for their time and feedback: Professor Wen Wang, Professor Dion Khodagholy, and Professor Nanfang Yu.

I would like to acknowledge past and present members of CLUE. In particular, I would like to thank Aida Raquel Colón-Berríos for your advice and expertise in the lab.

I would like to thank Dennis Wang for the countless dinners, coffee breaks, and hours spent studying together.

Finally, I would like to acknowledge the rats who gave their lives for the advancement of science.

Dedicated to Jenny Choi and Jae Kyu Choi

# Chapter 1

## Introduction

Recent progress in flexible electronics and sensors have shown promise for enabling a new class of wearable and implantable healthcare devices.[1, 2, 3, 4, 5, 6, 7, 8] By coupling advanced hardware with novel computational methods to collect larger sets of data with higher granularity than ever before,[9, 10, 11] it may be possible to greatly improve healthcare diagnostics and patient care, as well as our understanding of human physiology. One application in particular that can greatly benefit from advances in clinical hardware sensors is the diagnosis and treatment of epilepsy.

### 1.1 Epileptic Seizures

Epilepsy is a chronic neurological disorder which afflicts nearly 50 million people worldwide.[12] A patient is diagnosed with epilepsy when they have two or more unprovoked seizures that are not the result of another medical condition such as fever or drug withdrawal. While seizures can occur for a variety of reasons other than epilepsy, the causes for epilepsy itself are not well understood, as each case of epilepsy has its own distinct history and response to treatment.[13]

Seizures typically manifest as an excessive, hypersynchronous firing of a population of neurons in the cerebral cortex, the largest and most anterior section of the brain.[14] The cerebral cortex is divided into left and right hemispheres that serve major sensory, motor, and cognitive functions (Figure 1.1). There are three major categories of seizures: focal seizures, generalized seizures, and unclassifiable seizures.[15] Focal seizures are those that originate within a neuronal network that is limited to one cerebral hemisphere, whereas generalized seizures involve networks in both cerebral hemispheres. [15, 14] Focal seizures can evolve into generalized seizures if the seizure activity spreads from neuronal networks in one hemisphere to both.[15] The external symptoms of a focal seizure that has evolved into a generalized seizure are difficult to distinguish and are commonly only identified by electroencephalography (EEG) study. Subcategories of generalized seizures can include those of absent seizures where the patient experiences brief lapses of consciousness and atonic seizures where a sudden loss of posture can occur. Unclassifiable seizures are those that cannot yet be designated as either focal or generalized without further study.[15]

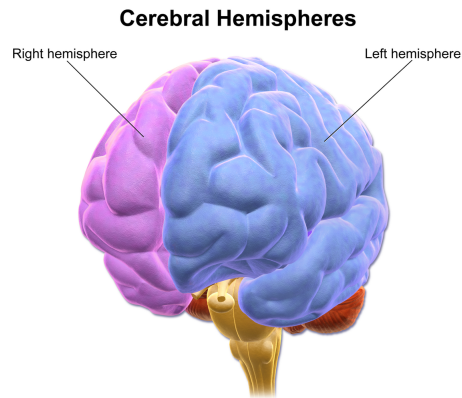


Figure 1.1: Diagram of the cerebral hemispheres.[16] Image courtesy of blausen.com staff (2014). "Medical gallery of Blausen Medical 2014". WikiJournal of Medicine 1 (2). DOI:10.15347/wjm/2014.010. ISSN 2002-4436. Reused under the Creative Commons Attribution 3.0 Unported license <https://goo.gl/KfFFfo>

### 1.1.1 Seizure Propagation and Treatment

Focal seizures can typically initiate in localized regions of the cortex and propagate to neighboring regions. According to *Harrison's Principles of Internal Medicine*, "The initiation phase is characterized by two concurrent events in an aggregate of neurons: (1) high-frequency bursts of action potentials and (2) hypersynchronization. The bursting activity is caused by a relatively long-lasting depolarization of the neuronal membrane due to influx of extracellular calcium ( $\text{Ca}^{2+}$ ), which leads to the opening of voltage-dependent sodium ( $\text{Na}^+$ ) channels, influx of  $\text{Na}^+$ , and generation of repetitive action potentials. This is followed by a hyperpolarizing afterpotential mediated by  $\gamma$ -aminobutyric acid (GABA) receptors or potassium ( $\text{K}^+$ ) channels, depending on the cell type." [15] With normal, healthy neuronal activity, hyperpolarization and surrounding inhibitory neurons prevent the propagation of the bursting activity; however, with sufficient activation by an increase of ion concentrations, enhanced neurotransmitter release, excitation of amino acid receptors, or stimulation of the neuronal tissue, neighboring neurons can be recruited for the propagation of seizures to contiguous areas of the cortex or to distant areas via pathways such as the corpus callosum.

The most common treatment method for epilepsy is through antiepileptic drug (AED) therapy, with the primary goals of reducing the frequency or eliminating seizures to the greatest extent possible, evading adverse side effects of long term treatment, and aiding patients in maintaining normal social, vocational, and lifestyle function. [13] Typically, AED therapy works by blocking the initiation or propagation of seizures. [15] The most common drugs used for inhibiting epileptic seizures may achieve this by inhibiting  $\text{Ca}^+$  channels in the neurons [13] or by increasing the presence of neurotransmitters that mediate synaptic transmission, such as gamma aminobutyric acid (GABA). [13]

Unfortunately, approximately 30% of patients with epilepsy do not respond to antiepileptic drugs. [13, 14] For these patients, the unpredictability of seizures occurring dramatically impacts the quality of life for both patients and caregivers. [17] One of the only alternative treatments for patients who are unresponsive to AED is epilepsy surgery which removes or disconnects pathology sections of brain matter.

Patients are eligible for resective epilepsy surgery if the areas of the brain responsible for seizures are safe to remove without overly severe levels of disruption to neurological function.[14, 15] In order to maximize the success of surgery, patient selection is critical. Surgeons employ thorough diagnostic tests including video and EEG monitoring, neuroimaging, and neuropsychometric studies. [14] Once a patient has been selected for surgery, extensive chronic study by neural imaging is required to identify the pathology areas of the brain and develop a surgical treatment plan. Thus, the development of high fidelity, high spatiotemporal resolution neural imaging capabilities are crucial for increasing the success of epilepsy surgeries, as well as furthering the understanding of complicated neurological disorders like epilepsy.

### 1.1.2 Mapping Neural Activity

Clinical practice currently measures neural activity via EEG and Electrocorticography (ECoG). These techniques utilize a grid of surface electrodes which measure the electrical local field potential of cortical neuronal dendrites near the brain’s surface. The electrical signals are conducted through the surface of the skull or cerebral cortex, for EEG and ECoG respectively. When neuronal cells activate, the flow of ions through the synapse creates a dipole outside the dendrite. The oscillation of electric field potential due to these dipoles can then be detected by the surface electrodes used in EEG and ECoG. While an EEG electrode placed on the scalp is unable to pick up single neuron activity, they are able to detect the potential changes due to clusters of thousands of neurons firing synchronously. [14]

For surgical candidates, ECoG recorded with a subdurally implanted array of surface electrodes covering a large surface of the brain is the standard of care for determining the focus and propagation of seizures (Figure 1.2). Typical studies prior to surgery involve long-term monitoring of neural activity with an implanted ECoG array lasting up to a few weeks, in addition to acute studies involving short-term implantation coupled with neural stimulation.[14, 15] While clinical ECoG measurements have improved resolution (typically  $<1$  cm and  $<1$  ms) and signal-to-noise ratio (SNR) over EEG, a greater spatiotemporal resolution and SNR of neural activity measurements would greatly aid treatment by surgical resections where even small errors on the order of 1 mm can be significant.[18]



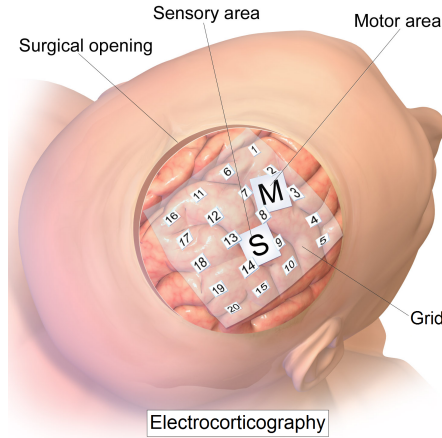


Figure 1.2: Schematic diagram of ECoG measurement using a subdurally implanted array of surface electrodes.[16] Standard clinical surface electrodes can perform chronic measurement of neural activity, but have relatively low spacial resolutions ( $< 1$  cm). Image courtesy of: Blausen.com staff (2014). "Medical gallery of Blausen Medical 2014". WikiJournal of Medicine 1 (2). DOI:10.15347/wjm/2014.010. ISSN 2002-4436. Reused under the Creative Commons Attribution 3.0 Unported (CC BY 3.0) license <https://goo.gl/KfFFfo>

## 1.2 High Resolution Imaging

Standard clinical methods for high resolution imaging include magnetic resonance imaging (MRI), positron emission tomography (PET), single photon emission computed tomography (SPECT), and magnetoencephalography (MEG), and functional MRI (fMRI). [14] While these techniques can produce maps of neural imaging with high spatial resolutions ( $< 1\text{mm}$ ) and are valuable for acute studies, these methods are not ideal for chronic studies as patient movement is restricted and functional dyes are required for some of the mentioned techniques.

Research in the field of advanced ECoG has sought to improve the resolution and fidelity of subdurally implanted surface electrode arrays with advances in both the sensing hardware[19, 20, 21] and computational analysis[9] involved. For instance, recent work by Khodagholy et al. has introduced a flexible, organic electronics-based array with interelectrode spacing as small as  $23\text{ }\mu\text{m}$ . [20, 21] These advances coincide with recent progress in the field of wearable and implantable flexible electronic sensors which holds much promise for future advanced and personalized healthcare diagnostics. [22, 1, 6, 23, 7, 8, 24, 4]

### 1.3 Optical Recording of Intrinsic Signal (ORIS)

A promising alternative to ECoG imaging of neural activity is the optical recording of intrinsic signal (ORIS). ORIS monitors changes in optical signals associated with neuronal activity.[25] By monitoring optical reflectivity changes caused by cerebral blood volume (CBV) and cerebral blood flow (CBF), seizure events in the brain have been recorded with high spatiotemporal resolution ( $<200\text{ }\mu\text{m}$  and  $<200\text{ ms}$ ). [26, 27, 28, 29] By taking advantage of the absorbance spectra of oxygenated and deoxygenated hemoglobin (Figure 1.3),[30] total CBV can be recorded by measuring the reflectivity of light at the isosbestic, or equal absorption, wavelengths for hemoglobin. Since, the brain is tightly vasoregulated, seizure events which induce exaggerated neuronal activity in localized regions of the brain are correlated with drastic changes in CBV and CBF that can be precisely mapped using ORIS. Work by Suh et. al demonstrated 2D mapping of seizure activity with spatial resolutions below  $200\text{ }\mu\text{m}$  using a suspended CCD camera to capture reflected ORIS signals.[29]

While ORIS can provide high spatiotemporal resolution imaging of seizure activity without the need for harmful dyes, an ORIS measurement system for clinical and long-term monitoring of neuronal activity has not been demonstrated. ORIS measurements using a suspended camera require the patient to be stationary, with their brain exposed. Early work in developing an implantable measurement system includes an ORIS sensor that uses off-the-shelf light emitting diodes and photodetectors integrated on a flexible substrate.[31] This semi-flexible device is able to perform seizure detection by ORIS with high signal-to-noise ratio (SNR), but is limited by the large dimensions of the components used. These

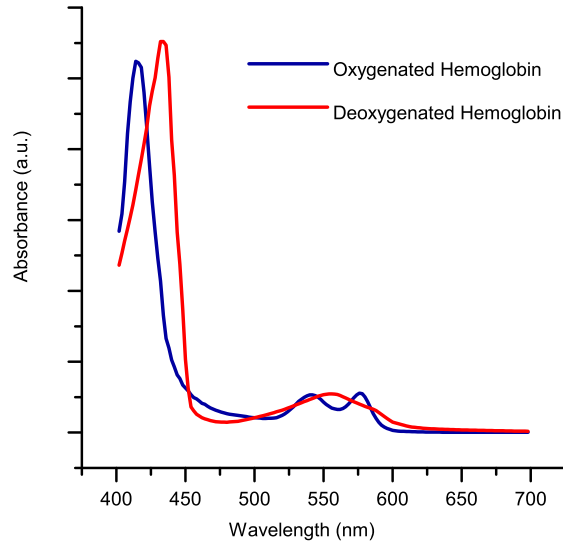


Figure 1.3: Hemoglobin absorbance spectra. Measuring reflectivity of light at isosbestic wavelengths where oxygenated and deoxygenated hemoglobin absorb light equally gives a relative measure of total CBV. The devices in this work target the isosbestic points at 449 nm, 522 nm, and 548 nm. Absorbance data provided by Prahl, et al.[30]

constraints limit the practicality of the device for comfortable subcranial implant, as well as the density of imaging elements needed to achieve high spatial resolutions.

## 1.4 Objectives and Approach

The objective of the work presented here is to advance the development of a subcranially implantable ORIS sensor for performing acute and chronic measurement of neuronal activity. An implantable ORIS sensor has the benefit of being practical for clinical applications, in addition to having improved seizure detection capabilities due to the active optical elements being in closer proximity to the surface of the brain. The requirements of such a device include: a soft and flexible biocompatible substrate for comfortable and safe implantation, a bright emitter for providing light input, a responsive photodetector for capturing subtle changes in optical reflectivity, and long operating lifetimes. In order to achieve device performance that meets these criteria, several novel display technologies have been adopted

for use in ORIS sensing. Two main device architectures presented here are: 1) an optical sensor based on flexible organic light emitting diodes and organic photodiodes 2) an optical sensor that utilizes microLEDs embedded on a flexible polyimide substrate with modification via quantum dot optical down-conversion.

## Chapter 2

# Basics of Flexible Optoelectronics

### 2.1 Introduction

This chapter reviews the basic operating principles of various flexible electronic and optoelectronic technologies used in this work. The primary elements involved in the development of an implantable ORIS sensor are a stable, bright emitter in the form of a light emitting diode (LED) and a photosensitive detector. While the use of flexible LEDs has been extensively studied for display and communication applications, the adoption of these devices for biomedical sensing is relatively new. A schematic showing the basic operating principles of an implantable ORIS sensor is shown in Figure 2.1.

### 2.2 LEDs and Photodiodes

Standard p-n junction diodes involve doped p-type semiconductor, where holes are the majority mobile charge carrier, abutted against an n-type material, where electrons are the majority mobile charge carrier. At zero bias, a depletion region of space charge forms on either side of the p-n interface due to charge diffusion. In the steady state, the electrostatic fields from the space charge in the depletion region prevent further diffusion of charge across the junction. In reverse bias, the depletion region is widened and practically no current flows, except at extreme voltages where device breakdown occurs. Under forward bias, charge injection causes the depletion region to narrow, until a significant amount of charge

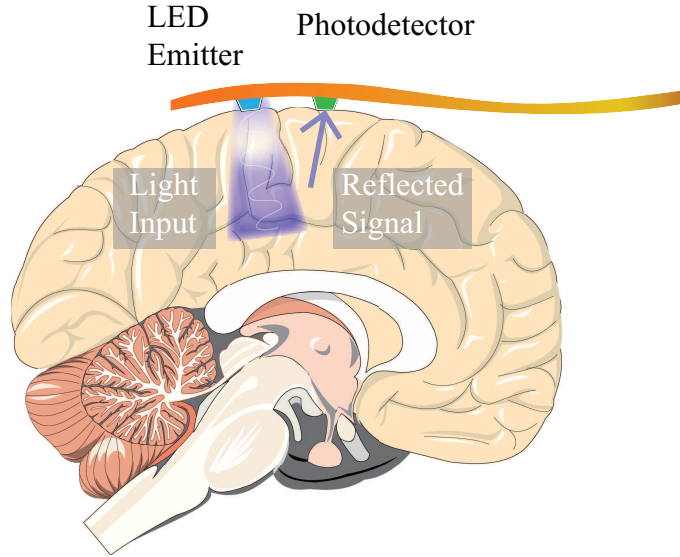


Figure 2.1: Schematic showing the design and operation of an implantable ORIS sensor. The primary elements include an LED and a photodetector integrated on a thin, highly flexible substrate.

is able to diffuse across the junction at bias voltages above the threshold. Thus, current is restricted to flow in one direction across the diode.

LEDs operate similarly to standard p-n junction diodes, except that the recombination that occurs at the interface between the n-type semiconductor and p-type semiconductor under forward bias is radiative, resulting in the generation of photons (Figure 2.2). Since LEDs are fabricated from mostly transparent materials, the light produced by recombination at the interface, can escape. LEDs conventionally are made from direct band gap materials like GaAs or GaN, which have higher probabilities of radiative recombination than indirect band gap materials. The wavelength of light emitted by an LED is determined by the bandgap of the emissive material where recombination occurs.

Photodiodes generally operate in reverse of LEDs. Light incident on the photosensitive material generates charge separation which is collected by the anode and cathode of the device. LEDs can operate like photodiodes, according to the Mims effect,[32, 33] but have larger bandgaps which diminishes the available range of wavelengths for producing photocurrent. Photodiodes can be operated in photovoltaic mode (no electrical bias) or

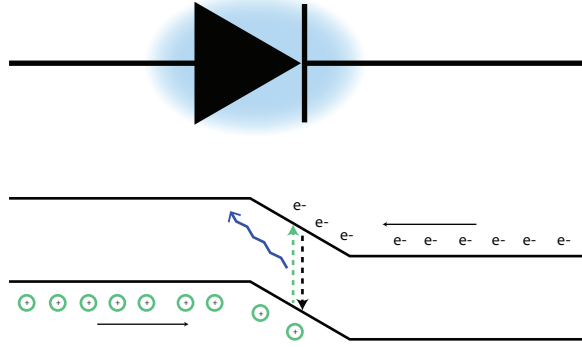


Figure 2.2: Schematic diagram of an LED. Radiative recombination in the p-n junction results in light emission at photon energies equal to the bandgap.

photocurrent mode (under a reverse bias). Photocurrent mode can increase the response time of the detector, but may introduce more electrical noise.

Conventional LEDs and photodiodes are typically very rigid due to the crystalline semiconductor materials they are made of, as well as the typical glass and sapphire substrates that are used for such devices. Silicon and other crystalline materials can be made flexible by using techniques such as wafer thinning and fabrication of silicon nanoribbons,[34, 35] but high performance devices are challenging to fabricate and are not intrinsically biocompatible. Hematoxylin- and eosin-stained histological

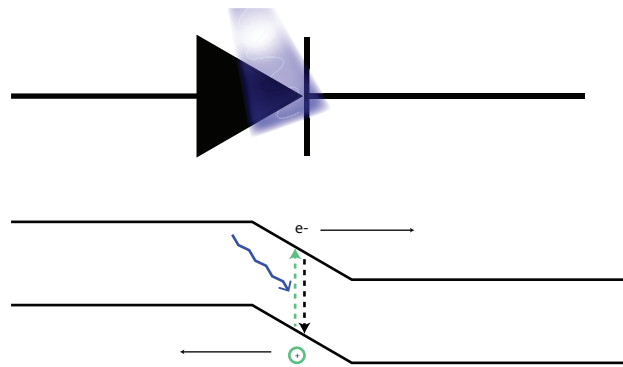


Figure 2.3: Schematic diagram of a photodiode. Incident light on the photodiode creates charge separation due to the photoelectric effect. The charges are swept towards the contacts due to the intrinsic electric field, generating a photocurrent.

## 2.3 Organic Semiconductors

One method of producing flexible electronics devices is to utilize organic semiconducting materials. Organic semiconductors are comprised of organic (containing carbon) small molecules or polymers and have the advantage of being intrinsically flexible, partly due to the thin nature of most organic electronic devices, with the total thickness of the active materials typically under  $1\text{ }\mu\text{m}$  ). Due to the fact that bonds between organic molecules tend to be weak, often formed by van der Waals interactions, thermal budgeting for processing and fabricating thin film organic semiconductors is low.[36] Therefore, organic semiconductor devices can be fabricated on almost any substrate, including plastics that cannot handle the intense thermal processing needed for many inorganic crystalline semiconductors. Organic semiconductors can even be fabricated by solution processing, an area of great interest for applications such as roll-to-roll processing and large area fabrication.[36]

Charge transport in organic semiconductors typically occurs via chains or sheets of  $\text{sp}^2$ -hybridized carbon. The electronic configurations of carbon atoms in organic semiconductors often form hybrid  $\text{sp}$  molecular orbitals which collectively have a lower energy than if the carbon molecules remained in their neutral valence electron configuration ( $2\text{s}^2, 2\text{p}^2$ ). Shared  $\text{sp}^2$  orbitals in carbon-carbon bonds form what are known as  $\sigma$ -bonds which are strong and highly directional.[36] Perpendicular to the axis of the  $\sigma$ -bonds, electrons in the weakly associated  $\text{p}_z$ , or  $\pi$ , orbitals of the hybridized carbon form what are known as conjugated  $\pi$ -bonds. These delocalized  $\pi$ -electrons can organize into multiple electronic configurations for a single type of molecule; an example of this is naphthalene whose conjugated bonds are depicted as alternating single and double bonds in Figure 2.4. These delocalized charge carriers in the  $\pi$ -bonds allow for charge transport in organic semiconductors.



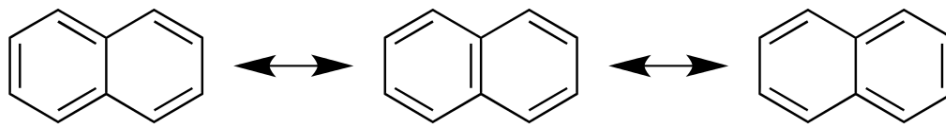


Figure 2.4: The resonance forms of naphthalene. The alternating double and single bonds form conjugate pairs, with the extra electrons forming the double bonds not having a specific localized orientation. This charge conjugation is the mechanism which gives rise to charge transport and semiconducting properties of organic semiconductors.

Charge transport in disordered organic materials is often described by “hopping” mechanisms, where the carrier lifetimes are short, resulting in charge mobilities which are typically smaller than inorganic crystalline semiconductors.[36] Also, unlike inorganic semiconductors which can transport both positive and negative charge carriers, many organic materials only support charge transport for one kind of charge carrier. Rather than n-type and p-type material designations which refer to doping in inorganic semiconductors, different types of organic semiconductors are referred to as hole transport (HTL), hole injection (HIL), hole blocking (HBL), electron transport (ETL), electron injection (EIL), and electron blocking (EBL) layers based on their charge transport characteristics. In OLEDs, the layer where radiative recombination occurs is also called the emissive layer (EML).

For organic molecules, a network of these conjugated molecular orbitals form, some of which may or may not be filled depending on the energy state of the molecule. Analogous to the conduction band of inorganic semiconductors, electrons are transported along the lowest unoccupied molecular orbital (LUMO). Holes are transported along the highest occupied molecular orbital (HOMO), similar to the valence band of inorganic semiconductors. The energy gap,  $E_g$ , between HOMO and LUMO is analogous to the band gap of inorganic semiconductors and is generally related to the conjugation length of the organic molecule chain. Typically, the longer the conjugated network, the smaller  $E_g$  is.

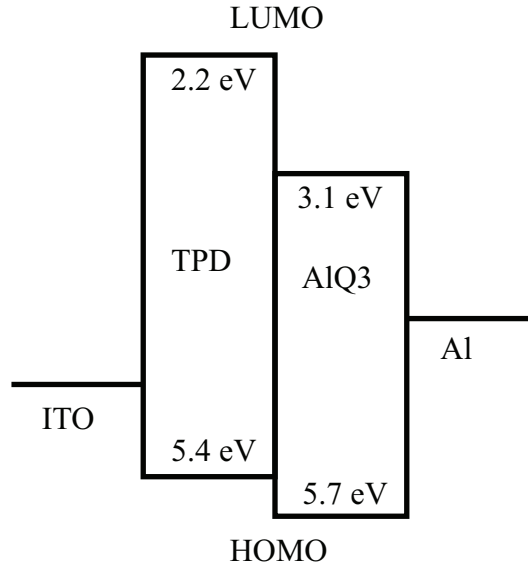


Figure 2.5: Example of the band structure of an OLED. Recombination in the EML results in green light emission whose wavelength is determined by the HOMO-LUMO gap of AlQ<sub>3</sub>.

### 2.3.1 Organic LED (OLED)

OLEDs are formed using electroluminescent organic semiconductor materials. OLEDs are commonly produced by stacking thin films of organic semiconducting material to form a heterojunction structure similar to a p-n junction. An example of the band diagram for an OLED heterojunction is shown in Figure 2.5.[37] The device stack is as follows: indium tin oxide (ITO) is used as a transparent anode, n,n'-bis(3-methylphenyl)-n,n'-diphenylbenzidine (TPD) forms the HTL, tris(8-hydroxyquinolato)aluminium (AlQ<sub>3</sub>) forms the EML/ETL, and aluminum forms a reflective cathode.

#### Efficiency

The efficiency of an OLED is a measure of a device's ability to convert electrical energy into light. The internal quantum efficiency refers to the ratio between charge converted into light due to recombination and the total number of injected charge during forward bias. Internal quantum efficiency can be calculated as:

$$\eta_{int} = \gamma \zeta_s q$$

$\gamma$  is the charge carrier balance.  $\zeta_s$  is the exciton generation efficiency, i.e. the efficiency for exciting charge carriers into singlet (for fluorescence and phosphorescence) and triplet (for phosphorescence only) excited states.  $q$  is the fluorescence quantum efficiency, or the efficiency of generating photons from excited singlet or triplet states depending on whether the OLED is fluorescent or phosphorescent.[38]

Singlet and triplet states refers to the excited charge states that occur according to the pauli exclusion principle, where no two electrons occupying the same orbital can have the same magnetic spin state. In the ground state, two electrons occupying the same orbital must have opposite spins from each other. This configuration is called the singlet ground state (Figure 2.6). When light is absorbed by one of the electrons, they are excited to an orbital with higher energy. If the spin state of the excited electron is preserved during the transition, it is in a singlet excited state. If the spin state has been reversed and the spins of both the unexcited electron and the excited electron are now aligned in parallel, it is called a triplet state. Singlet-to-triplet and triplet-to-singlet transitions are typically far less likely to occur due to the need for a spin transition on top of the usual energy absorption. Fluorescent OLEDs are only able to produce light emission by singlet to singlet-state-transitions. Excited singlet states can relax to triplet excited states by intersystem crossing, but these transitions tend to have longer relaxation times and don't result in radiative emission for fluorescent OLEDs. Thus, the theoretical maximum efficiency for a fluorescent OLED is 25% since light emission only occurs via 1 out of 4 available excited states (1 singlet excited state and 3 triplet excited states).[38] Phosphorescent OLEDs tend to include heavy metal structures which allow for photon emission by both triplet-to-singlet relaxation and singlet-to-singlet relaxation. Therefore, phosphorescent OLEDs have a theoretical maximum efficiency of 100%.[38, 39, 40]

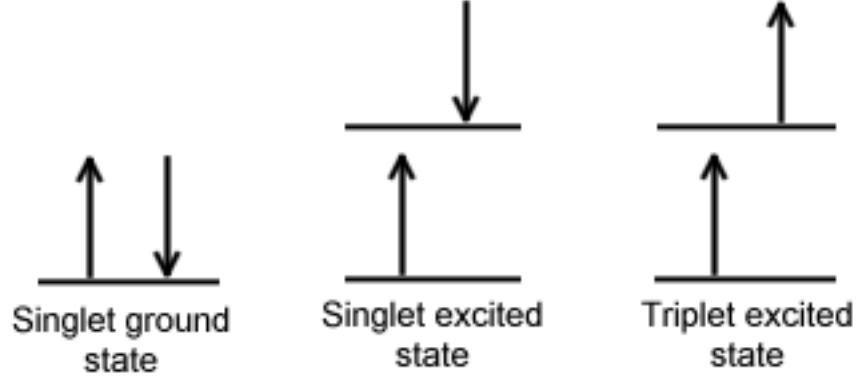


Figure 2.6: Diagram of singlet and triplet excited states.

External quantum efficiency (EQE) is the efficiency of converting injected charge into photons that can be extracted as light emission and provides a more useful metric for device performance. In addition to the same factors involved with internal quantum efficiency, EQE also takes into account the ability of the device to outcouple light. EQE can be calculated with the following equation:

$$\eta_{ext} \cong \eta_o \gamma \zeta_s q$$

, where  $\eta_o$  is the outcoupling efficiency of the device. Outcoupling efficiency can be affected by the choice of substrate, device thickness, device geometry, among many other factors. One method, among many, of improving outcoupling efficiency is by integrating a microlens into the device or substrate in order to improve light extraction and enhance directionality of the emitted light.[41, 42]

## Pathways of Degradation

A chief concern with the use of OLEDs is the relatively short operational lifetimes. The organic materials and electrodes used are vulnerable to oxidation and moisture-related degradation when exposed to atmospheric conditions. For this reason, OLEDs are typically fabricated and assembled in inert environments, such as nitrogen or argon filled gloveboxes. Lifetime of OLED devices are usually quantified by measuring the luminance over time, during constant operation. One standard metric for the lifetime is the luminance half-life, or the time it takes for an OLED's luminance to decay to half of its initial value.

Environmentally caused degradation to the device often manifests in dark spots,[43] which decrease their luminance. Dark spot generation can be caused by local oxidation of the cathodes, microscopic shorting between the electrodes due to localized heating and morphological defects, charge accumulation at layer interfaces, and other structural defects or damage.[44, 45, 38, 46] Lifetime can be improved by simply improving the efficiency of the device, reducing the thermal and electrical stress placed on the OLED.[46, 43] Furthermore, environmental factors on device lifetime can be mitigated by using encapsulation or hermetic sealing, providing a barrier against harmful oxygen and moisture.[44, 47] For flexible OLED applications, flexible encapsulation schemes can also involve alternating stacks of deposited thin barrier films.[48, 49, 50]

### 2.3.2 Organic Photodetector (OPD)

Organic photodiodes (OPDs) and organic solar cells operate similarly to their silicon counterparts. Instead of n-type and p-type semiconductors, the photosensitive materials that form the junction in OPDs are called electron acceptors and electron donors. When light is absorbed by charge carriers in organic materials, an exciton (bound electron-hole pair) with binding energy,  $E^{binding}$ , is formed, rather than free charge carriers as with inorganic photodetectors.[51] In order to generate photocurrent, the exciton binding energy must be overcome to convert the exciton into free charge, and monolayers of organic photosensitive material have poor efficiencies since the excitons are not easily converted to free charge and collected.[52, 51]

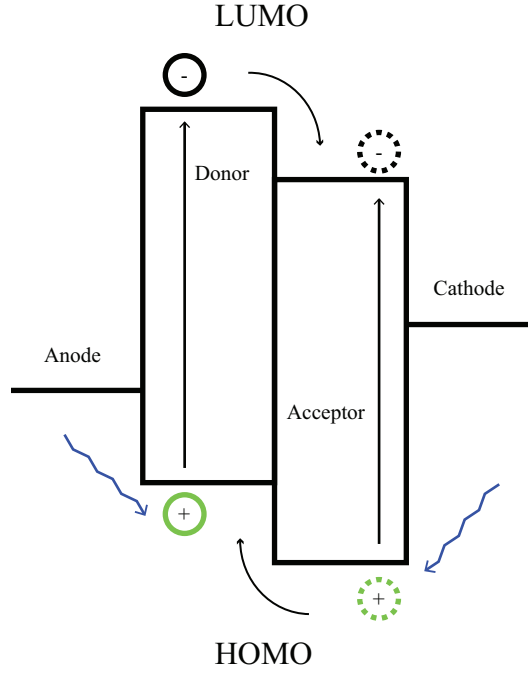


Figure 2.7: Photoexcitation and free charge conversion in a donor-acceptor junction.

One strategy of overcoming  $E^{binding}$ , is to create an electron donor/electron acceptor interface where charge transfer can occur after photoexcitation.[51] Electrons excited in the donor can transfer into the acceptor if the difference between the donor and acceptor LUMO levels (or electron affinities) is greater than  $E_D^{binding}$ , the exciton binding energy for the donor. Similarly the photogenerated holes in the acceptor can transfer into the donor if the difference between the donor and acceptor HOMO levels (or ionization potentials) is greater than  $E_A^{binding}$ , the exciton binding energy for the acceptor. To achieve high photoinduced charge separation yields, the photogeneration of excitons must occur within a diffusion length of the donor-acceptor interface.[53] One approach to maximizing the efficiency of OPDs is to create a bulk heterojunction device which has a blended donor-acceptor layer across the majority of the device.[54, 55]

## Responsivity and Efficiency

The internal quantum efficiency of the OPD device is the ratio of charge carriers collected at the contacts to the number of absorbed photons, whereas the external quantum efficiency (EQE) is the ratio of charge carriers collected at the contacts to the total number of incident photons on the OPD's active area. EQE is mainly determined by the efficiencies of the free charge generation and the absorption cross section of the device. Responsivity, or the extracted photocurrent divided by the incident light power, is related to EQE by :

$$R = EQE * \frac{\lambda q}{hc}$$

, where  $\lambda$  is the wavelength of incident light,  $c$  is the speed of light,  $h$  is planck's constant, and  $q$  is the electron charge. Responsivity is the primary metric for determining the practical effectiveness of an OPD for implantable ORIS sensors.

### 2.3.3 Fabrication Methods

OLEDs and OPDs are typically fabricated by either physical vapor deposition under high vacuum or by solution processing. While solution processing is appealing for applications like roll-to-roll processing and large area fabrication, it is typically more challenging than vacuum deposition since many organic materials are sensitive to solvents and high temperatures, and vacuum deposited OLEDs have traditionally had higher performance.[56] With those considerations, OLED and OPD stacks deposited by thermal evaporation under high vacuum tend to be patterned by shadow masking. With shadow masking, a hard stencil is used to cover areas where deposition of the evaporated material in question is not desired. One downside of vacuum deposition of organic device layers is the relatively long processing times related to placing the devices in high vacuum for deposition and frequent mask exchange for sophisticated heterojunctions.

### 2.3.4 Biomedical Applications for OLED and OPD

Examples of OLED and OPD technology used in biomedical applications follows. These examples use a variety of fabrication methods and detection schemes, displaying the versatility of OLED and OPD technologies applied to biosensors.

#### Organic Pulse Oximeter

Pulse oximetry is a noninvasive technique for optically measuring pulse and oxygenation of blood through the skin. Typically, an emitter and photodetector pair are attached to a body part, such as a fingertip or earlobe. Light at two wavelengths is transmitted through the body part and changes in light absorbance are recorded by the photodetector. Changes in the absorbance of the two wavelengths correspond to changes in oxygenated and deoxygenated hemoglobin, providing a measure of the current ratio of the two. An alternative technique measures changes in reflected light from the surface of the body to achieve the same diagnostic measurement.

An organic-based pulse oximeter was demonstrated by Lochner, et al. which replaced the inorganic LED and photodetector elements with flexible OLEDs and OPDs. [57] The OLEDs and OPD were fabricated using solution processing on a ITO-patterned glass substrate and a polyethylene naphthalate (PEN) substrate, respectively, which could be wrapped around a finger for performing transmissive pulse oximetry measurements. To fabricate this device, electrodes for the OLEDs and OPDs were formed by vacuum deposition. The active organic layers for the OLEDs were spin-coated, including a TFB:F8BT:TBT emissive layer for the red OLED and a TFB:F8BT emissive layer for the green OLED. The active layers for the OPD were blade coated, including a PTB7:PC<sub>71</sub>BM photosensitive layer. A schematic of the completed device and extracted pulse and oxygenation measurements are shown in Figure 2.8.

The solution processing techniques used to fabricate the device shows the potential for low cost, large area production of organics based wearable biosensors. Additionally, the ability to fabricate onto flexible substrates enables applications requiring the placement of the sensors on different areas of the body.



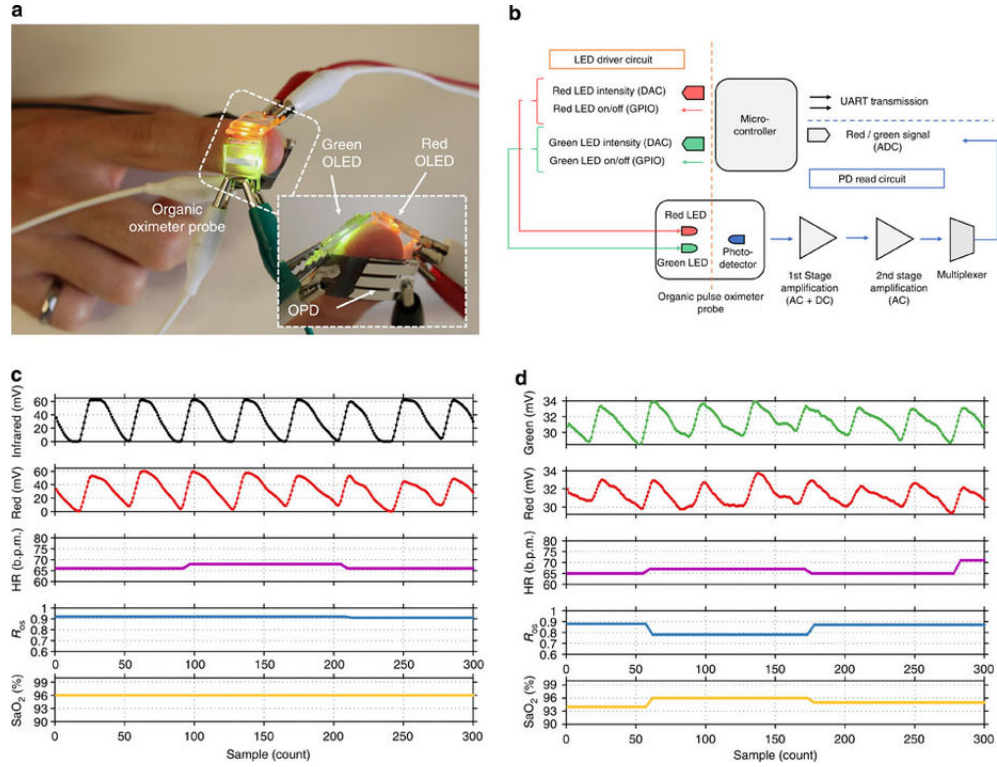


Figure 2.8: a) Organic pulse oximeter replaces inorganic optoelectronic elements with OLEDs and OPDs (b) Hardware block diagram for the system including amplification and a microcontroller for data acquisition (c,d) Simultaneous oximetry measurements with a commercially available inorganic oximeter probe and the organic oximeter probe, respectively. Heart rate is determined from the timing of the systolic peaks in the oximetry signals. The ratio of transmitted light at two wavelengths was used to calculate blood oxygen saturation using Beer–Lambert’s law. [57] Reprinted by permission from Lochner, Claire M., et al. "All-organic optoelectronic sensor for pulse oximetry." *Nature communications* 5 (2014): 5745.

### Miniature Laboratory-On-A-Chip Biosensor

Laboratory-on-a-chip (LOC) technologies which integrate sensors and devices onto an integrated circuit (IC) capable of performing complete laboratory measurements and functions are a potential solution for providing next generation point-of-care diagnostics requiring a compact physical footprint, portability, and ease of operation/automation. Wojciechowski, et al. demonstrated a microfluidic LOC biosensor with an integrated OPD for performing chemiluminescence (CL) detection of a toxin, Staphylococcal enterotoxin B (SEB). [58] CL detectors record light emissions from chemical reactions that lead to photoexcitation and are used for immunoassays and nucleic acid detection. [59] These detectors do not require a light source as only a photodetector is needed to measure the photoemission from the chemical reactions, decreasing the footprint and complexity of the devices.

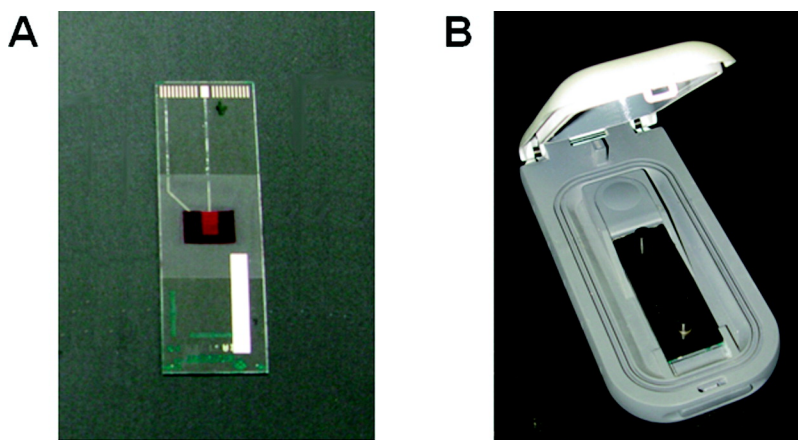


Figure 2.9: Miniaturized biosensor using OPDs. [58] a) A glass slide with a printed OPD sensor is used for CL detection of SEB b) The glass slide is placed into a portable controller for data acquisition. Reprinted with permission from Wojciechowski, Jason R., et al. "Organic photodiodes for biosensor miniaturization." *Analytical chemistry* 81.9 (2009): 3455-3461. Copyright 2009 American Chemical Society."

The OPD based CL detector, shown in Figure 2.9, consisted of an OPD printed onto a glass slide with an active area of 4 x 4 mm and a quantum efficiency of 50-60% at the 532 nm wavelength. A sandwich immunoassay was performed directly onto the OPD slide, where the slide was coated with  $\alpha$ -SEB capture antibody, then exposed to SEB, and incubated with horseradish peroxidase (HRP)-conjugated  $\alpha$ -SEB tracer antibody ( $\alpha$ -SEB-HRP) . An opaque microfluidic chamber was attached to the sensor, and the slide was placed into a portable OPD controller for data acquisition.

A representative measurement curve is shown in Figure 2.10. A SEB treated substrate was added  $\sim 20$  s into the recording, after which a detectable signal  $\sim 300$  pA above the baseline of  $\sim 80$  pA was observed. A low limit of detection, enabled by the low dark current of the OPD, for measuring SEB concentration of this device was stated at 0.5 ng/mL. This limit of detection was comparable to CCD and PMT based detectors, demonstrating the ability to produce compact, high performance biosensors using OPDs. [59]

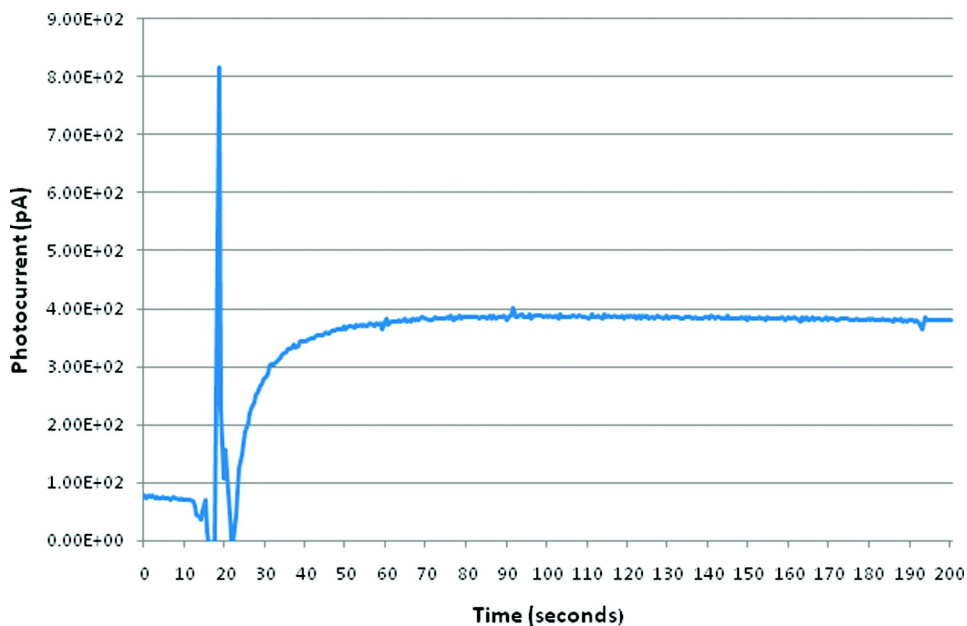


Figure 2.10: CL detection of SEB using an OPD. [58] Substrates treated with  $\alpha$ -SEB, SEB, and  $\alpha$ -SEB-HRP were added  $\sim 20$  s into recording. The concentration of SEB detected measured in this plot was 5 ng/mL. Reprinted with permission from Wojciechowski, Jason R., et al. "Organic photodiodes for biosensor miniaturization." *Analytical chemistry* 81.9 (2009): 3455-3461. Copyright 2009 American Chemical Society."

## 2.4 MicroLED

MicroLEDs are essentially inorganic LEDs, typically using nitride materials, that have been miniaturized. MicroLEDs can be fabricated monolithically into arrays, or they can be fabricated and released for pick and placement as individual elements in large arrays. The ability to individually control and address LED elements reaching dimensions under  $100\ \mu\text{m}$  has led to commercial interest in MicroLEDs for use in emissive displays, since they tend to have superior performance over OLEDs in terms of operating efficiency and lifetime. Recent advances in fabrication and processing of microLEDs has led to the availability of devices with high brightness, even at relatively low bias voltages.[60, 61, 62] Also unlike OLEDs which have relatively short operational lifetimes due to the degradation of the organic thin films used, operational lifetimes for microLEDs are very long in comparison due to their

inorganic composition. While these advantages in performance are ideal for use in long-term *in vivo* measurement of ORIS, the drawback of microLEDs is their intrinsic rigidity. Embedding microLEDs in a flexible circuit or substrate ultimately limits the flexibility of the final device. Additionally, the planar geometry of most microLED elements can lead to structural vulnerabilities when used in a flexible device architecture; however, this can be overcome with appropriate strain engineering. [63]

Work by Hong, et al. demonstrated a highly flexible display utilizing microLEDs assembled on printed rigid islands composed of poly (methyl methacrylate) (PMMA). [63] Printed rigid islands (PRIs) were embedded in PDMS forming a highly stretchable, soft substrate with a thickness of  $\sim 50 \mu\text{m}$ . Patterned electrode traces were then inkjet-printed onto the substrate, and microLEDs were soldered onto the PRIs. With this design, locally strain-free among the soft substrate existed where the microLEDs were attached, preventing detachment of the relatively flat and rigid microLED components from the flexible substrate. Completed devices are shown in Figure 2.11. The strain engineered design for these flexible microLED arrays provides a template for producing customized microLED arrays on highly flexible substrates. This method provides a robust technique for building a resilient substrate compatible with a wide variety of different microLED and other small, rigid optoelectronic components. Such properties are vital for creating optoelectronic sensors and implantable devices for biomedical applications.

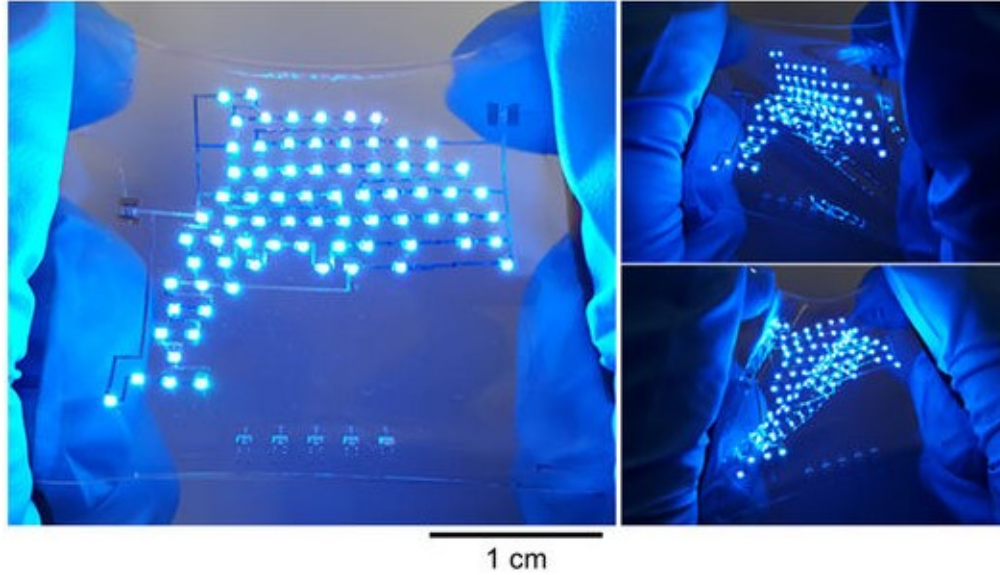


Figure 2.11: Strain engineered flexible microLED display. [63] Reprinted by permission from Byun, Junghwan, et al. "Fully printable, strain-engineered electronic wrap for customizable soft electronics." *Scientific Reports* 7 (2017): 45328.

MicroLEDs have found recent success in many fields of biomedical research. Some applications include: optogenetic stimulation,[64, 65] cochlear implant,[66], and biological fluorescence imaging.[67] . These demonstrations highlight the potential for microLED use in biomedical sensors, including wearable and implantable electronics.

Optogenetics, where light is used to control the stimulation or suppression of neuronal activity, represents a possible next generation treatment for neurological diseases such as epilepsy and Parkinson's disease. [68] Typically, genetic modification is used to introduce light sensitive proteins which drive specific, controlled actions in neurons with high temporal resolution. For optogenetic applications involving neuronal cells inside of the body or brain, MicroLEDs and microLED implants show great promise for implementing clinical optogenetic treatments requiring efficient light input in a compact package.

One successful application of microLEDs in this field was accomplished by Montgomery, et. al where a microLED implanted on the surface of a mouse's brain was operated completely wirelessly for optogenetic stimulation. [65] In this work, a commercial blue microLED was attached to a circuit for wireless power delivery. A mouse expressing channelrhodopsin 2 (ChR2) was implanted with the device and placed above a resonant cavity for RF wireless power delivery (Figure 2.12). When the microLED was powered on, the blue light emission activates ChR2, triggering a circling behavior in the mouse's movement. The setup was able to produce enough light input ( $1\text{-}20\text{ mW/mm}^2$ ) for ChR2 activation without excessive heating of the animal ( $< 1\text{ }^\circ\text{C}$  change in body temperature) by duty cycling under 40%. This achievement represents one practical approach to advanced healthcare for patients with neurological diseases utilizing implantable optoelectronic devices.

MicroLEDs used for ORIS measurements in this work are commercially available and are packaged as individual elements. The microLEDs have preformed AuSn solder bumps for eutectic die attach. This allows the chips to be placed on a substrate or circuit with a die bonder or via flip chip bonding, without the need for wire bonding or traditional soldering. Because of the thermal processing required to reflow the AuSn solder, substrates and materials that can withstand relatively high temperatures must be used. Additionally, the small footprint of the bond pads calls for the use of photolithographically patterned circuitry and bond sites, meaning the substrates used must be resistant to solvents and UV light exposure. This limits the available substrates and materials for use in flexible and implantable devices integrated with microLEDs.

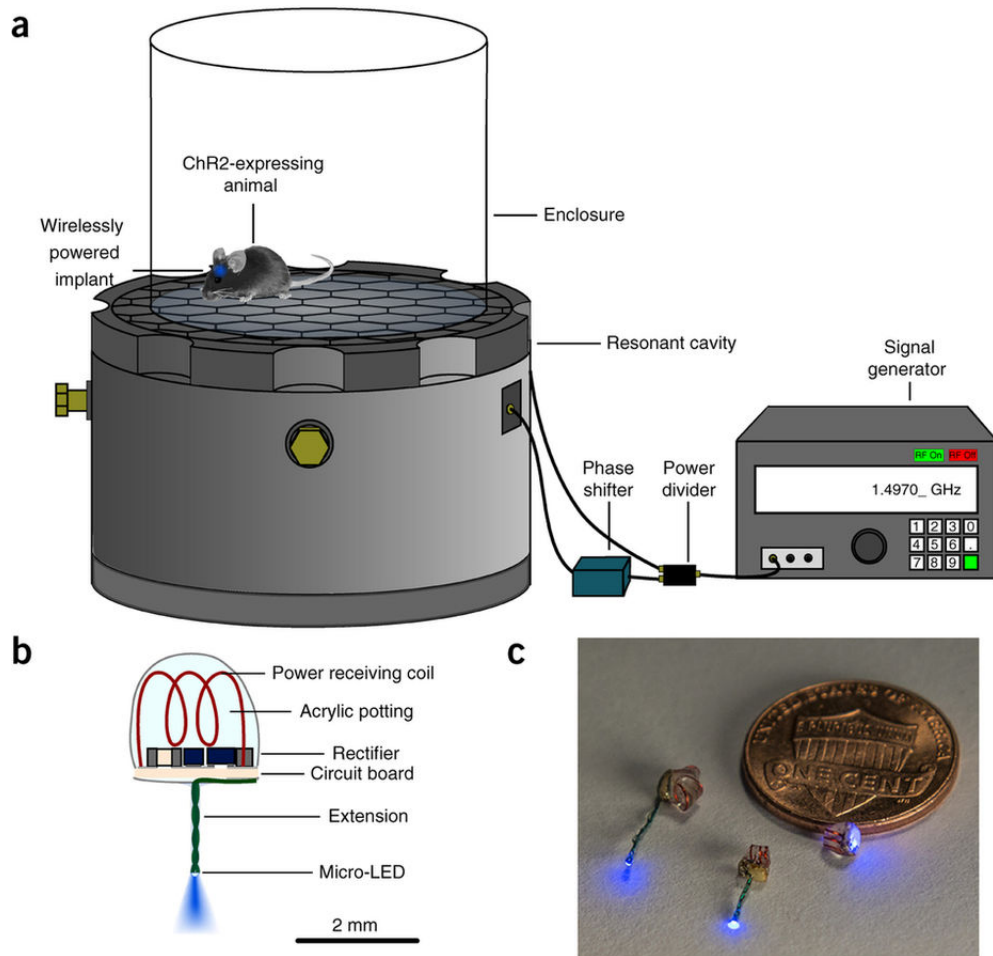


Figure 2.12: Wireless optogenetic stimulation of mice using a microLED implant a) A mouse implanted with the wireless blue microLED implant was confined to an enclosure containing a resonant cavity for wireless power delivery. The blue microLED was powered on wirelessly, triggering a circulatory motor behavior induced by the activation of ChR2 b) Schematic of the wireless microLED implant c) Photograph of the microLED implant [65] Reprinted by permission from Montgomery, Kate L., et al. "Wirelessly powered, fully internal optogenetics for brain, spinal and peripheral circuits in mice." *Nature methods* 12.10 (2015): 969-974.



## 2.5 Colloidal Quantum Dots

Colloidal quantum dots (QDs) are nanocrystals of semiconducting material produced by solution processing that exhibit quantum effects due to their small size. The optoelectronic properties of QDs are a function of their size and structure.[69, 70] Electrons in QDs behave much like “particles in a box” with quantum confinement effects in 3 dimensions.[70] The discrete electronic states that arise from confinement result in very sharp spectral qualities. As such, QDs have been adopted in many commercial displays and are being thoroughly researched for their potential applications in optoelectronics [71, 72, 73] and imaging biomarkers[74, 75, 76]. In particular the wavelength of emitted light can be tightly tuned with narrow spectra by adjusting their size and structure, but without changing the material composition.[73] This is a huge advantage over other optoelectronic devices which tend to have less tunable emission spectra heavily dependent on the material composition. The synthesis of QDs is discussed in the appendix.

### 2.5.1 Electroluminescent QDLEDs vs. Photoluminescent QDs

There are two variants of LED technology that takes advantage of QDs. The first is the electroluminescent quantum dot LED (QDLED), which operates similarly to an OLED. QDLEDs are comprised of a thin layer, often just a single monolayer, of QDs sandwiched between charge transport layers. Excitons in QDLED can occur by either photon charge injection, energy transfer, or by ionization of QDs.[73] The relaxation of these QD excitons results in electroluminescence at photon energies equal to the bandgap of the QD. The primary difference between different kinds of QDLEDs reside in the charge transport layers, which may be formed with organic, inorganic, or a hybrid mixture of organic and inorganic materials.[73, 71, 72]

Photoluminescent QDs differ from QDLEDs in that they are optically driven, rather than electronically driven. This is most commonly seen in displays where white or blue backlight is converted by a QD dye by absorption and re-emission.[77] Adopting QDs into other optoelectronic devices can enhance them by providing a level of wavelength tunability that is not normally available. This versatility is crucial in optimizing the performance of

implantable and wearable optoelectronic sensors and expanding their practical applications.

### **2.5.2 Biomedical Applications for Quantum Dots**

Examples of the use of QDs in biomedical applications follows. These examples take advantage of the unique optical properties of QDs for providing highly tunable narrowband light emission. The progress reported in these examples show the promise of future clinical therapies which utilize advanced materials such as QDs.

#### **Photodynamic Therapy**

Photodynamic therapies involve activating photosensitizers with specific wavelengths of light to destroy cancer cells, for example via reactive oxygen species (ROS). [78] Therapies involving external illumination for targeting cancer cells within the body are limited by the penetration depth of the light and may have undesired side effects due to photosensitivity of the skin. The use of nanotechnology to reduce or eliminate the required external irradiation has been a topic of interest in the development of photodynamic therapies.

Work by Hsu et al. demonstrated the use of QDs in targeted photodynamic therapy requiring zero external irradiation (Figure 2.13). [79] The QD-conjugate used in this work were composed of light-emitting Renilla luciferase 8 (RLuc8) proteins and carboxylate-containing QDs, which self illuminate via bioluminescent resonant energy transfer (BRET).[80] In the BRET process, energy is released from the RLuc8 substrate coelenterazine, electronically exciting the QD which then emit light. BRET was used to internally illuminate meta-tetrahydroxyphenyl-chlorin (m-THPC) photosensitizers in photodynamic therapy targeting the reduction of tumors (Figure 2.13).

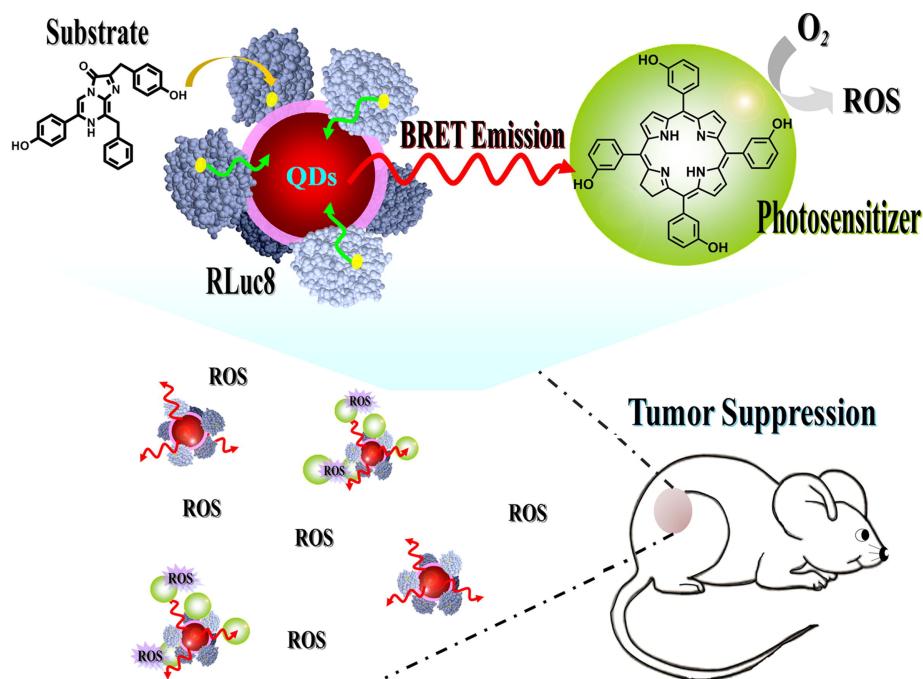


Figure 2.13: Schematic diagram of QDs used in targeted photodynamic therapy for tumor suppression. [79] Reprinted from Biomaterials 34.4, Hsu, Chia-Yen, et al., "Bioluminescence resonance energy transfer using luciferase-immobilized quantum dots for self-illuminated photodynamic therapy.", Pages 1204-1212, Copyright 2013, with permission from Elsevier.

The successful reduction of tumor volume by BRET-induced photodynamic therapy is shown in Figure 2.14. Mice were injected with different permutations of the QD-conjugate (QD-RLuc8), photosensitizer loaded micelles photosensitizer (m-F), and coelenterazine and then monitored for their tumor growth rates. For mice which received BRET-induced photodynamic therapy (having received the full QD-RLuc8/m-F/coelenterazine treatment), significant reduction of tumor volume was observed. This demonstrates the ability to use QDs for the internal activation of photosensitizers in photodynamic therapies. This kind of achievement may lead to effective clinical application of photodynamic therapies that utilize QDs without the need for external light sources and can extend to applications beyond photosensitizers that target cancer cells.

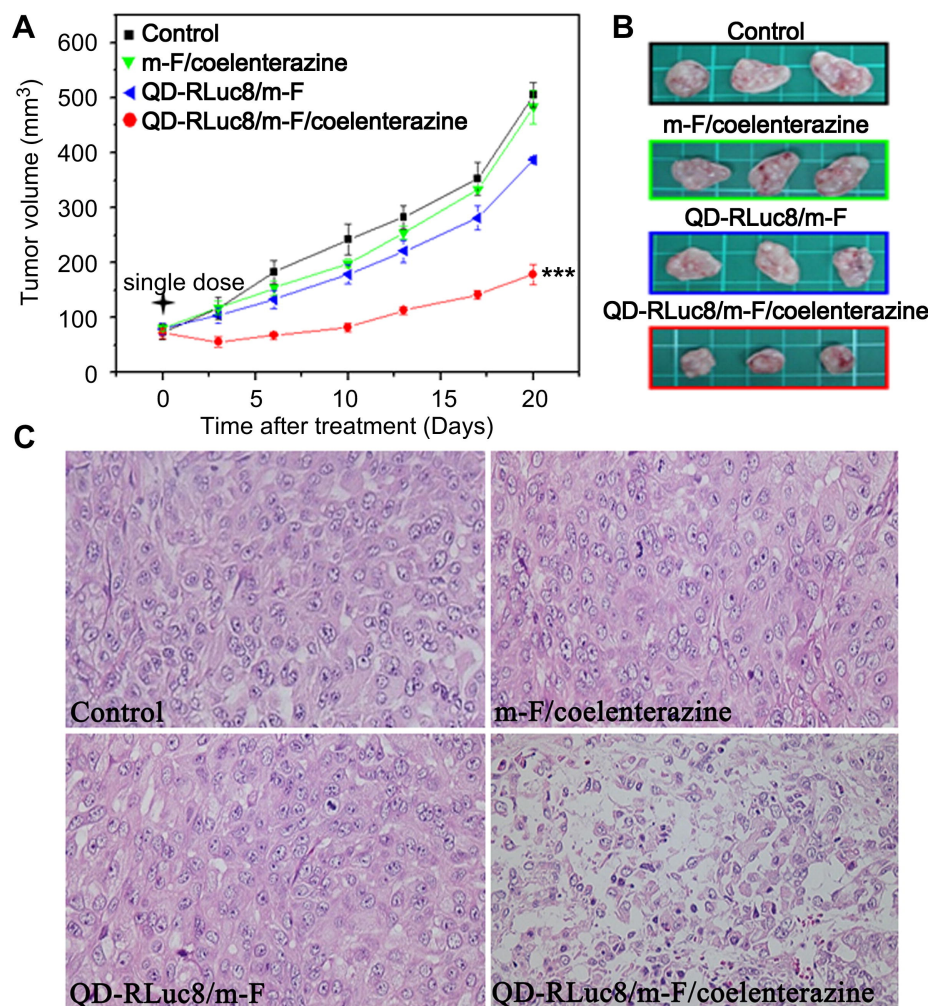


Figure 2.14: Tumor suppression via QD-enabled targeted photodynamic therapy.[79] a) Tumor volume was tracked for the different permutations of treatments. Mice which received the BRET-induced photodynamic therapy showed a reduction in tumor volume b) Stained sections of tumors c) Microscope image of tumors. Reprinted from Biomaterials 34.4, Hsu, Chia-Yen, et al., "Bioluminescence resonance energy transfer using luciferase-immobilized quantum dots for self-illuminated photodynamic therapy.", Pages 1204-1212, Copyright 2013, with permission from Elsevier.

## QDLEDs for Photobiomodulation

The use of electroluminescent (EL) QDLEDs in wearable devices and biomedical devices has gathered interest as QD technology has progressed both commercially and for research purposes. Chen et al. demonstrated the use of EL QDLEDs for photobiomodulation, in which light is used to stimulate cellular function. [81] Such treatments could potentially aid with wound recovery via applications such as light emitting bandages. In their work, QDLEDs which have brighter emissions at the necessary wavelengths (in the deep red region) were proposed as an alternative to OLEDs which have struggled to meet the performance requirements for such applications. The performance and structure of such QDLEDs is shown in Figure 2.15.

These highly efficient QDLEDs produced high brightness emission, up to  $165,000 \text{ Cd/m}^2$  at a peak emission wavelength of 620 nm.[81] In-vitro studies of these QDLEDs used in photobiomodulation therapy were performed using cell lines (HEp-2 [ATCC-CCL-2]; L929 [ATCC-CCL-1], 3T3 [ATCC-CRC-2593]) which act as surrogates for whole animal studies of wound healing. The QDLEDs were placed underneath cell culture wells containing the cell lines, and the QDLEDs were powered on for 10 min, illuminating the cell lines for photobiomodulation therapy (Figure 2.16). Assay results at 24 hours post treatment showed increased cell metabolism comparable to previous results achieved with inorganic LEDs (up to 27.9% increase for the HEp-2 cell line). [81] While improvements in performance for flexible QDLEDs of this type must be made in order to enable applications such as wearable or bandage based photobiomodulation treatments, the devices demonstrated in this work show the potential for utilizing the unique optical properties of QDs in wearable and implantable applications.

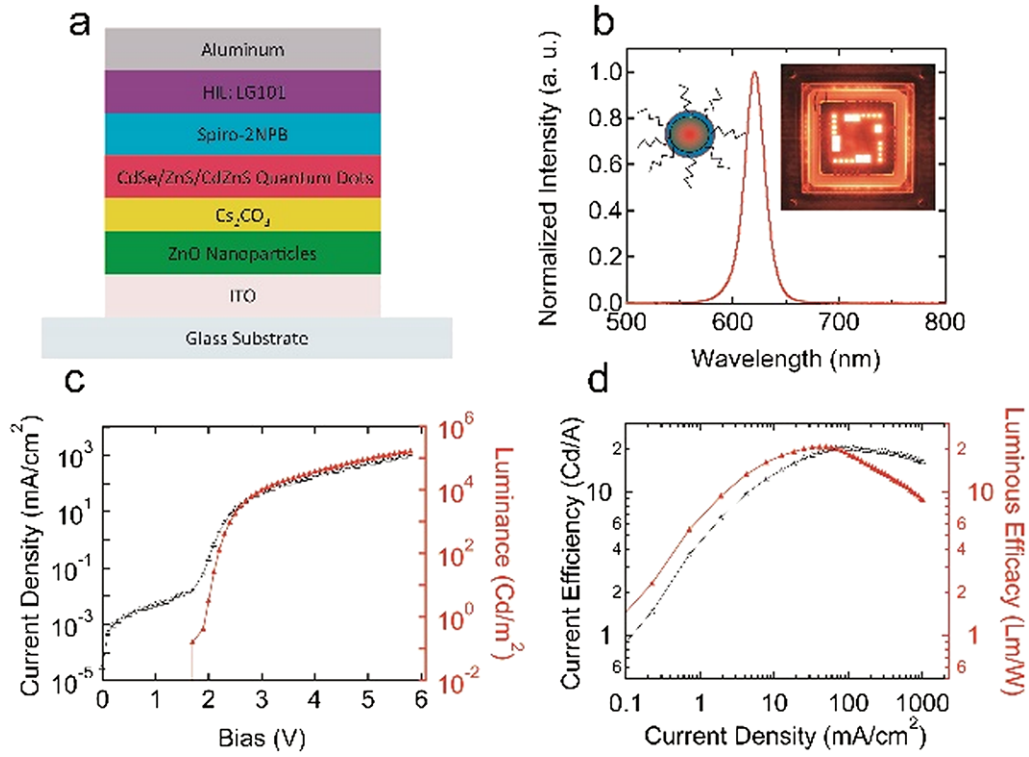


Figure 2.15: QDLED structure and performance. [81] a) Inverted QDLED structure b) Emission spectrum of the EL QDLED. Insets show the structure of the QD and a photograph of a completed QDLED c) Electroluminescent performance of the QDLED reported d) The QDLED is a high efficiency device capable of high brightness. Reprinted by permission from Chen, Hao, et al. "Quantum dot light emitting devices for photomedical applications." Journal of the Society for Information Display 25.3 (2017): 177-184.

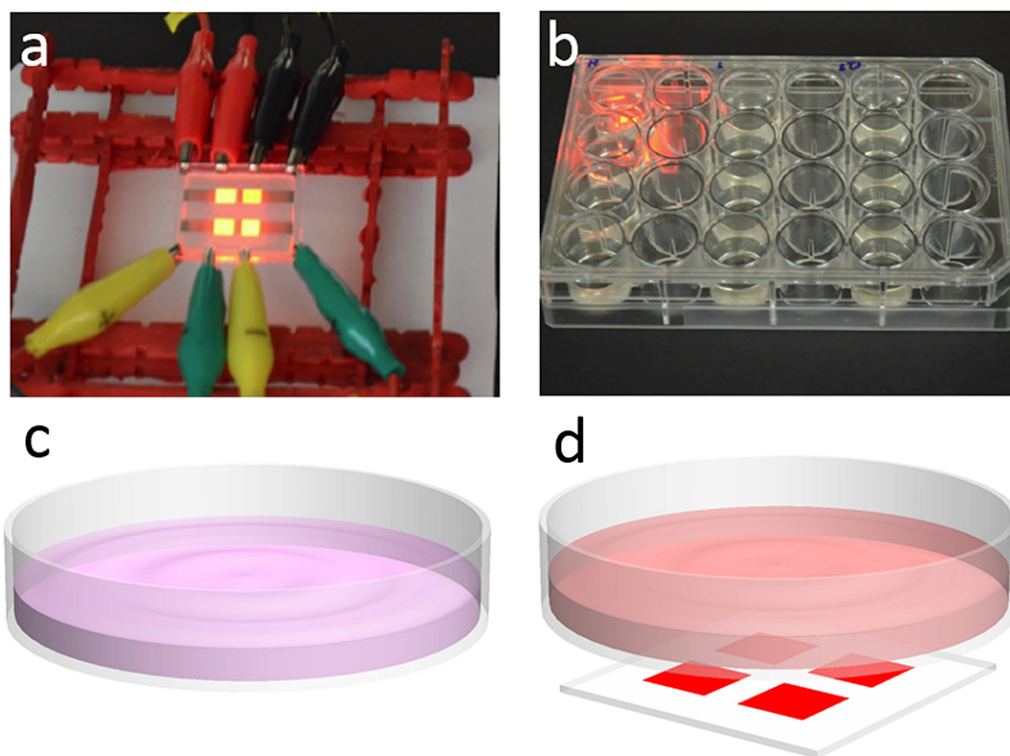


Figure 2.16: Photograph and schematic of the QDLED photobiomodulation therapy. [81]  
a) Photograph of the red QDLED with 620 nm peak emission b) The QDLED is placed underneath the transparent cell culture wells to perform in-vitro photobiomodulation therapy  
c) Schematic of the control experiment with no illumination d) Schematic of the cell lines receiving photobiomodulation therapy using a QDLED. Reprinted by permission from Chen, Hao, et al. "Quantum dot light emitting devices for photomedical applications." *Journal of the Society for Information Display* 25.3 (2017): 177-184.

## Chapter 3

# Integrated Organic LED and Organic Photodetector on a Highly Flexible Parylene-C Substrate

### 3.1 Highly flexible substrate

In order to achieve high levels of flexibility, a polymer based substrate was used. Biocompatible plastic substrates such as poly(ethylene 2,6-naphthalate) and poly(ethyl benzene-1,4-dicarboxylate), or PEN and PET respectively, are commonly used for flexible displays using OLEDs. However, the bending radius for these substrates are typically limited to around 5 mm.[82, 2] In order to achieve higher flexibility and conformal attachment, free-standing parylene-c is used as the substrate and encapsulation. Parylene (poly(p-xylylene)) is a polymer, deposited by chemical vapor deposition, which is often used for barrier coatings and biocompatible membranes/interfaces.[83] Parylene-c is the variant of the parylene polymer which has one chlorine group per repeat unit (Figure 3.1). Conformal coatings of parylene-c are chemically and electrically inert, biocompatible films,[84, 85] ideal for passivating the devices and protecting them from the environment of the brain.



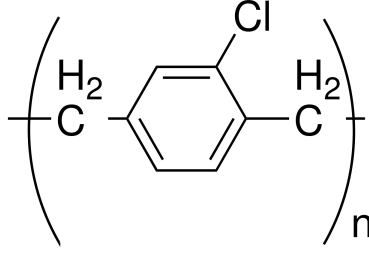


Figure 3.1: Parylene-C Structure

### 3.2 OLED and OPD Structure

The device used in this chapter consists of an OLED and OPD fabricated on a flexible substrate (Figure 3.2).[86] A phosphorescent tris[2-phenylpyridinato-C2,N]iridium(III)-based ( $\text{Ir}(\text{ppy})_3$ ) OLED was used.[39] The higher quantum and electrical efficiency of phosphorescent OLEDs over fluorescent OLEDs results in higher light output and longer operational lifetimes of OLEDs.[40, 43] The structure of the OLED stack is shown in Figure 3.2. The electron blocking layer (EBL) consists of molybdenum trioxide ( $\text{MoO}_3$ ). A layer of 4,4'-bis(N-carbazolyl)-1,1'-biphenyl (CBP) is doped with  $\text{Ir}(\text{ppy})_3$  to form the hole transport (HTL) and emissive (EML) layer where phosphorescent charge recombination occurs. Bathocuproine (BCP) forms the electron transport layer (ETL), and a thin layer of lithium fluoride (LiF) acts as a hole blocking layer (HBL). The photosensitive heterojunction of the OPD is formed by copper(II) phthalocyanine ( $\text{CuPc}$ ), a metallic-organic semiconductor often used in organic photovoltaics, and fullerene ( $\text{C}_{60}$ ).[87, 88]  $\text{MoO}_3$  forms the EBL followed by  $\text{CuPc}$  donor and  $\text{C}_{60}$  acceptor layers. BCP forms the ETL with a thin LiF HBL.

The OLED and OPD pixels are 0.5 mm x 0.5 mm in dimension and are spaced apart by 0.8 mm. By applying state-of-the-art commercial fabrication processes for patterning the OLED and OPD. Smaller pixel sizes and spacing between elements may be achieved for sub-millimeter imaging resolutions over a large surface area. The OLED is a bottom-emitting device with a semi-transparent gold anode on the bottom of the stack. The OPD similarly has a semi-transparent anode on the bottom of its stack.

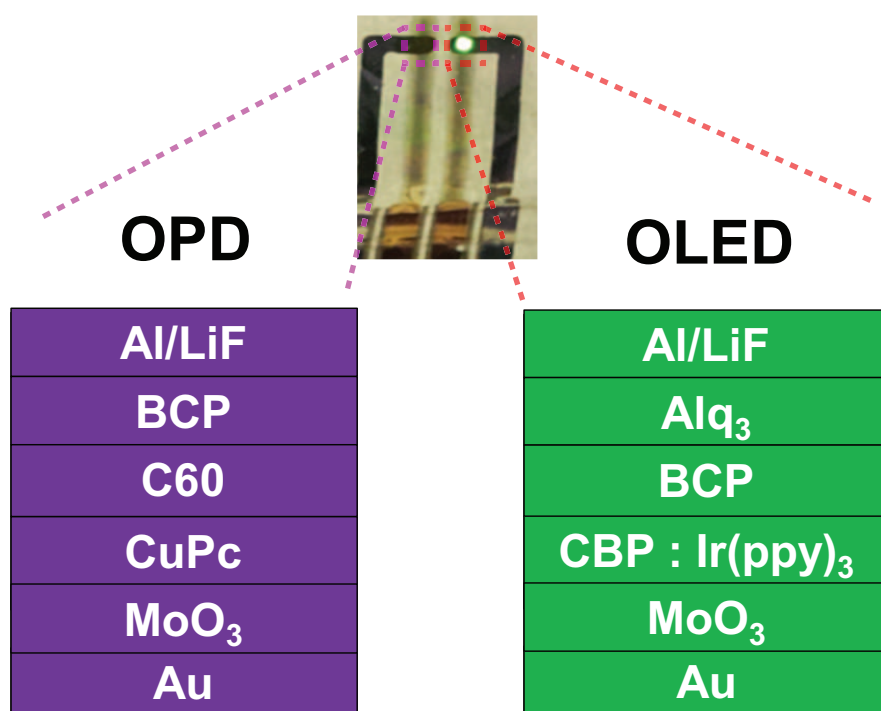


Figure 3.2: Schematic of the OLED and OPD structure. A photograph showing the layout of the OLED and OPD on the ORIS device is shown.

### 3.3 Fabrication

First, glass slides are cleaned by sonication baths in dilute soap (Micro-90) solution, acetone, and isopropyl alcohol (IPA) in that order for 15 minutes each. Next, 2  $\mu\text{m}$  of parylene-c are deposited via CVD to form the bottom encapsulation and substrate. The substrates are transferred to a nitrogen filled glovebox and into an evaporator housed within the glovebox. Then 40 nm gold anodes are deposited via thermal evaporation at a rate of 0.4  $\text{\AA}/\text{s}$ . At thicknesses below 50 nm, gold forms flexible, semi-transparent electrodes. Since organic semiconductors are typically sensitive to solvents and high temperatures, the patterning of electrodes and material stacks are carried out via shadow masking.

The organic layers for the OLED are then thermally evaporated under high vacuum.  $\text{MoO}_3$  /  $\text{CBP}:\text{Ir}(\text{ppy})_3(10\%)$  / BCP /  $\text{Alq}_3$  / are deposited in that order. After a mask exchange, the organic layers for the OPD are thermally evaporated adjacent to the OLED stack.  $\text{MoO}_3$  /  $\text{CuPc}$  /  $\text{C}_{60}$  / BCP are evaporated and deposited in that order. Finally, 1nm LiF is and 100 nm of aluminum are thermally evaporated to form a hole blocking layer and cathode for both the OLED and OPD. A layer of copper is evaporated over the areas where the metal traces are eventually contacted to provide mechanical support and allow the traces to withstand the contacting process.

After the OLEDs and OPDs have been completed, the devices are transferred immediately to the parylene coater to receive a top coating of 2  $\mu\text{m}$  parylene-c. Vinyl hard masks are used to protect the contacts from being insulated by the parylene. After the hard masks are removed, the electrodes are contacted via hot bar bonding with heat seal connector. The completed devices are then mechanically exfoliated from the glass carriers and tested. The entire fabrication process is shown in schematic in Figure 3.3. This device architecture also allows for the incorporation of more complex substrates and encapsulation layers involving alternating stacks of parylene-c and oxide films, which have been shown to improve operating lifetimes of OLED devices. [89]

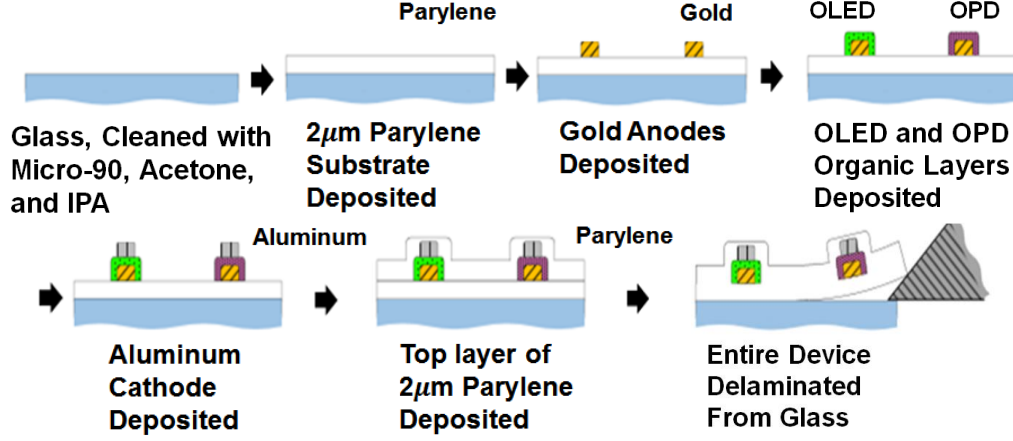


Figure 3.3: Fabrication of Organic Implantable ORIS Sensor

### 3.4 Device Performance

The resulting ORIS devices fabricated on free standing parylene membranes are less than  $5\text{ }\mu\text{m}$  thick and exhibit high flexibility (Figure 3.4). The thin profile and high flexibility of the device ensures that it will be able to comfortably be implanted underneath the skull. Additionally, the thin substrate minimizes cross-talk between the emitter and detector. Figure 3.4b shows the device bending around a wire with an  $80\text{ }\mu\text{m}$  diameter while emitting green light. The device is also shown operating after being wrinkled (Figure 3.4c) and exposed to saline solution (Figure 3.4d). The device can also attach to wet surfaces that have arbitrary geometries without the need for adhesive, as seen in Figure 3.4e.

The  $\text{Ir(ppy)}_3$  based OLEDs have a peak emission wavelength  $540\text{ nm}$ , which overlaps with an isosbestic point of hemoglobin (Figure 3.5). The OPD used in the device has a broadband spectral response with an effective range between  $450\text{ nm}$  and  $700\text{ nm}$  (Figure 3.6). This allows the same OPD to be used for detection at non-isosbestic wavelengths in addition to the  $540\text{ nm}$  isosbestic point, enabling the measurement of other biosignals such as oxygenation. The OPD is operated in photovoltaic mode (zero electrical bias). Under these conditions, the OPD has a responsivity over  $3.6\text{ A/W}$  (3.7). The ratio of dark current (no illumination) to photocurrent during exposure to green LED light is over 1500. This responsivity means the OPD is highly sensitivity to changes in reflectivity necessary for

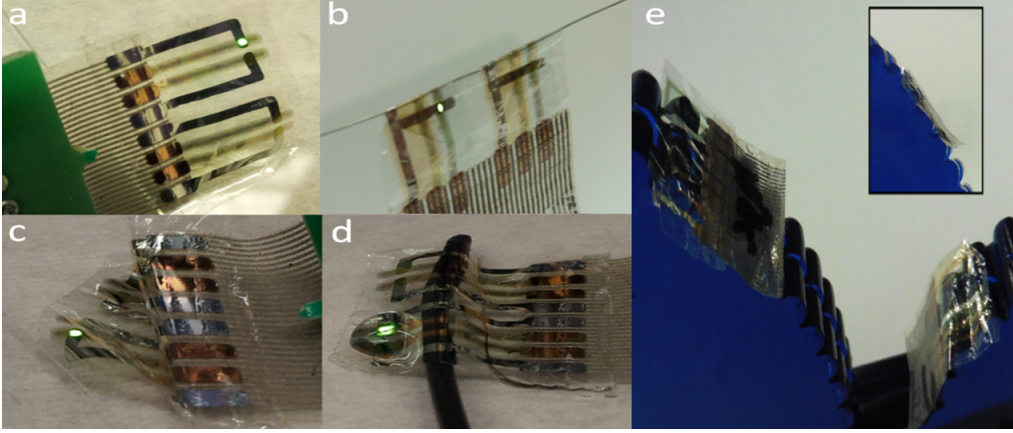


Figure 3.4: Flexible ORIS Sensor

performing ORIS measurement.

During the ORIS measurement, the OLEDs are supplied with a constant current between  $50 \mu\text{A}$  and  $100 \mu\text{A}$ . At these current densities, the light emission is on the order of  $\sim 100 \text{ cd/m}^2$  with voltages on the order of  $\sim 8.2 \text{ V}$  (Figure 3.8), more than sufficient brightness for performing the ORIS measurements while attached to the surface of the brain. The operational lifetime of the OLED is shown in Figure 3.9. The operating lifetime of the device is dominated by the OLED's performance since the OPD receives zero electrical bias and thus experiences significantly less electrical stress. To test the lifetime of the OLEDs, the OLEDs are supplied with a constant current, while the emitted luminance is measured with a luminance meter (Konica Minolta LS-10). The lifetime of the OLED is defined as the time it takes for the luminance of the OLED to decay to half its initial value. The test is carried out both in atmospheric conditions in air and while the devices are immersed in saline solution, to simulate the wet conditions of the brain. The lifetime of the devices in the aqueous conditions is over an hour, which is sufficient for performing acute measurements of seizures and neural activity. While the lifetime is not long enough to perform chronic measurements of epilepsy, where the patients need to be monitored for days or weeks at a time, the lifetimes of the device can be improved by introducing encapsulation layers into the parylene-c substrates[89].

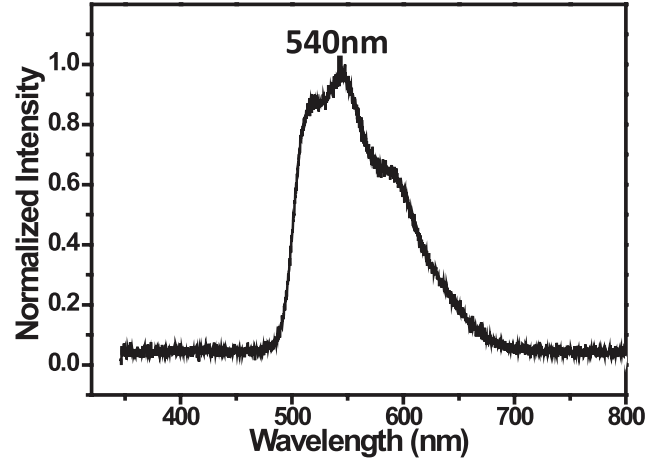


Figure 3.5: OLED Emission Spectrum . The emission spectrum has a peak emission at 540 nm which overlaps with an isosbestic wavelength for hemoglobin.

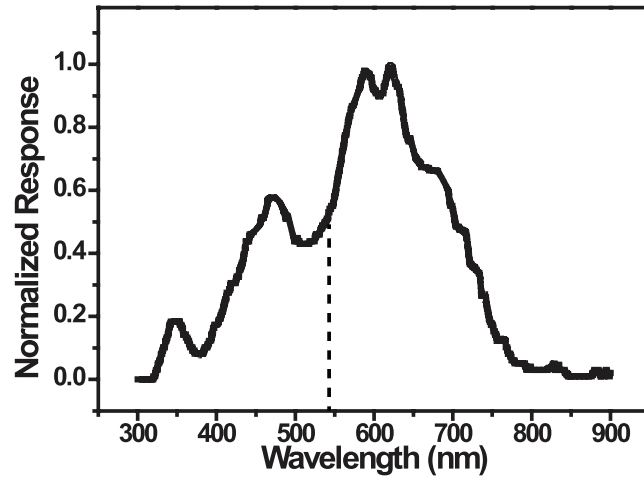


Figure 3.6: Normalized Spectral Response of OPD . The 540nm isosbestic wavelength used in the ORIS measurements is denoted with a dashed line.

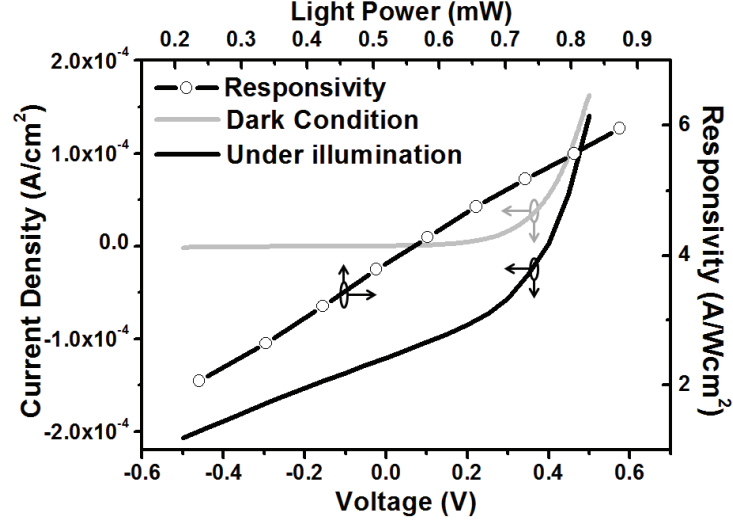


Figure 3.7: OPD Photocurrent Response. The ON/OFF ratio between photocurrent generated under illumination and the background current under dark conditions is over 1500

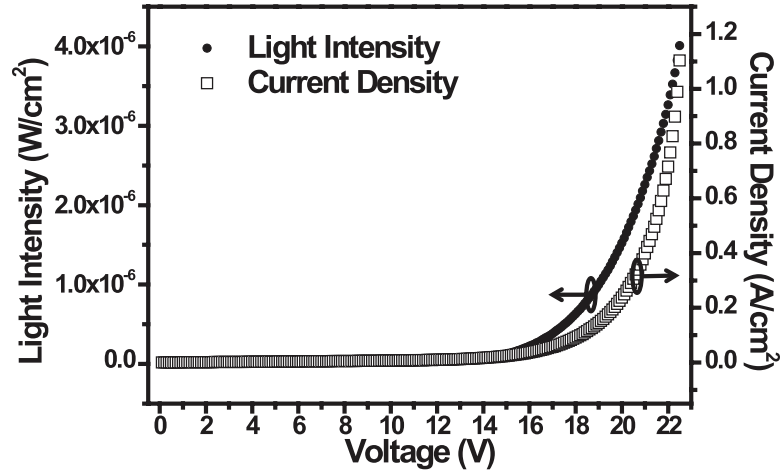


Figure 3.8: OLED Electrical Current and Light Output. With a bias voltage of 8.2 V, the OLED outputs  $5.6 \mu W$  of light, roughly  $100 \text{ cd/m}^2$ .

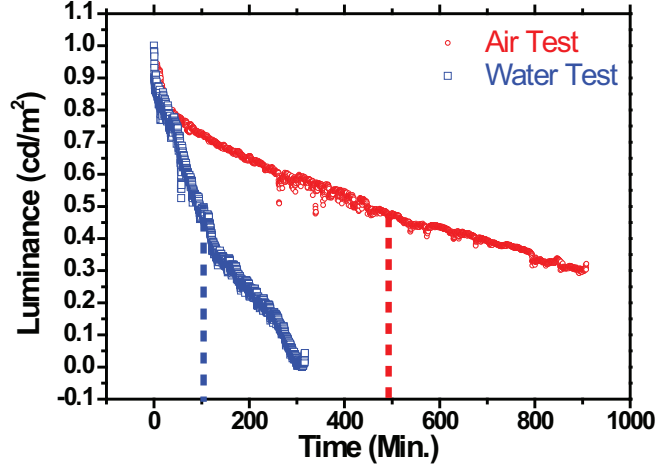


Figure 3.9: OLED Operational Lifetime. The luminance half-life is marked with a dashed line. The device has a lifetime over an hour when exposed to saline solution.

### 3.5 *In Vivo* Measurement of Neural Activity and Detection of Seizures

The organic-based ORIS device records *in vivo* measurement of cerebral blood volume (CBV) on the surface of a rat's brain. The rat is anaesthetized and the brain is surgically exposed for attachment of the ORIS device. A needle electrode measuring the local field potential (LFP) as a reference signal for neural activity is implanted near the ORIS device's site of attachment (Figure 3.10). The OLED is then powered to produce light input into the brain tissue, while the photocurrent generated in the OPD by the reflected light is recorded by an analog-to-digital converter. The photocurrent is amplified using a current amplifier whose output is recorded by an analog to digital converter.

Baseline variations of CBV are measured, including hemodynamic changes due to the heartbeat, respiration, and slow sinusoidal harmonic oscillations in the brain of the animal (Figure 3.11). A fast Fourier transform (FFT) shows the heartbeat and respiration with frequencies of 5.7 Hz and 1 Hz respectively. After baseline measurements are recorded, 4-aminopyridine (4AP) is locally injected into the brain via the needle electrode, inducing



epileptic-like seizures. Figure 3.12 shows the ORIS device's ability to detect seizures, which are highlighted by . The presence of a seizure is confirmed by the exaggerated oscillations in the LFP. At the onset of seizure, the drastic increase in neural activity triggers a hemodynamic response which results in a large flow of blood to the regions of the brain affected by the seizure. The increase in CBV means more of the light input from the OLED is absorbed and a decrease in the reflected OI signal (around 10% drop in the OI signal is observed, during each seizure). As the neural activity returns to the baseline, the CBV in the area returns to normal, and the OI signal increases back to the baseline. This behavior is observed for every seizure that occurs during the recording session, demonstrating the reliability of this technique as an alternative to ECoG detection of seizures.

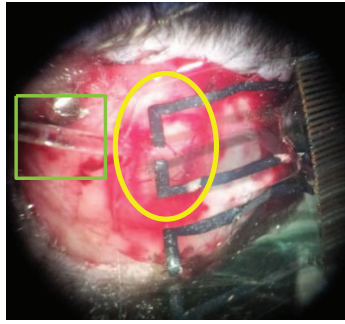


Figure 3.10: Photo of the organic ORIS device attached to the surface of the brain. The OLED and OPD elements are circled in yellow, while the needle electrode is marked by a green box.

### Baseline Variations in Optical Signal

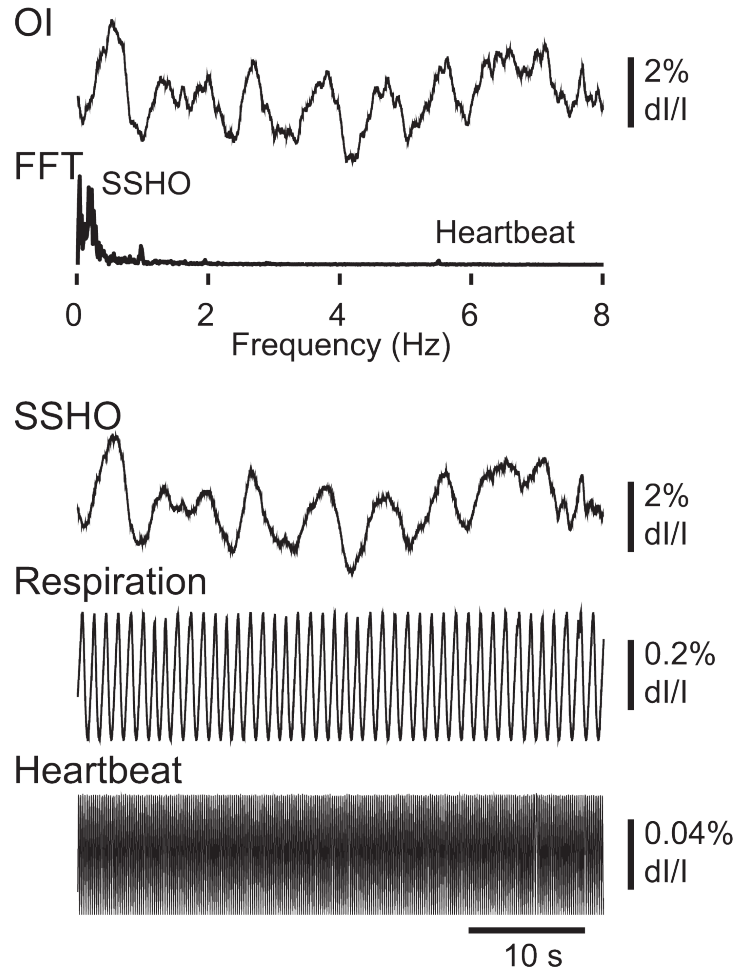


Figure 3.11: Baseline variations in the CBV of the animal's brain recorded by the organic ORIS device. The optical intrinsic (OI) signal captured by the organic ORIS device is shown at the top with a fast Fourier transform (FFT) of the OI shown directly below it. Isolated signals of SSH0, respiration, and heartbeat are extracted from the OI signal by notch filtering and plotted.

### Seizure Induced Optical Signal

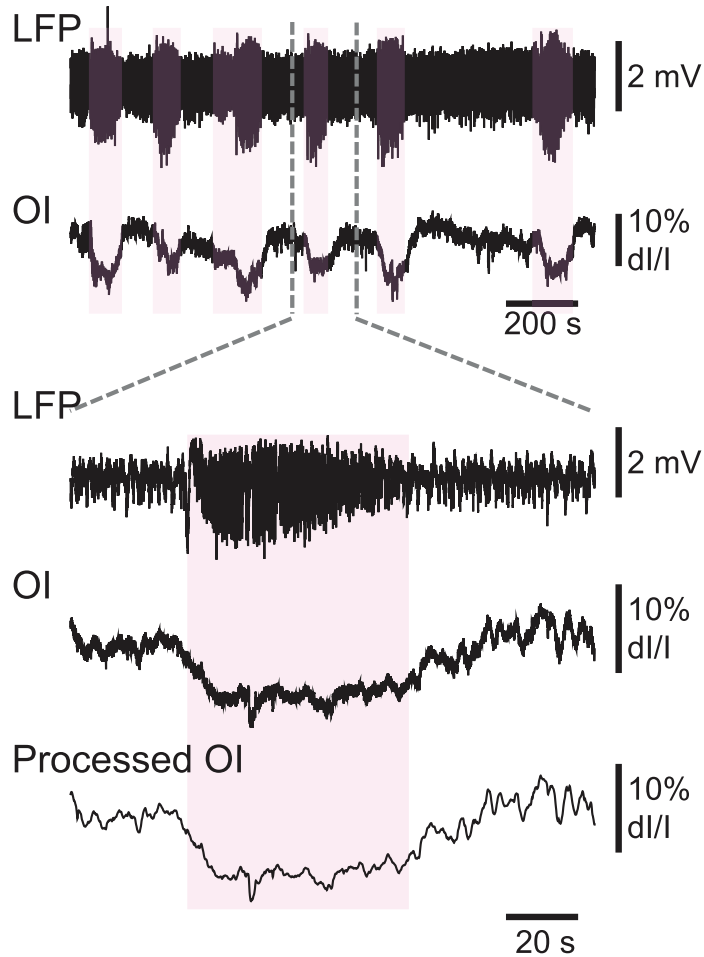


Figure 3.12: *In vivo* seizure detection using the organic ORIS device. The two plots at the top show the LFP and OI signal recorded simultaneously during a sequence of seizures. The duration of seizures is shaded in pink. A more detailed view of a single seizure that occurred in the middle of the sequence is shown below. The processed OI signal was produced by removing the oscillations due to heartbeat and respiration, a significant source of noise in detecting seizures.

### 3.6 Chapter Summary

In this chapter, an organic-based implantable ORIS sensor for *in vivo* detection of seizures was discussed. The complete device included OLEDs and OPDs fabricated on a biocompatible, free standing parylene-c substrate with a total thickness under 5  $\mu\text{m}$ , including encapsulation. The flexibility, performance, and seizure detection ability of the device was discussed, demonstrating the potential for application as a clinical alternative to ECoG measurement of neural activity.

## Chapter 4

# MicroLED Based Sensor

### 4.1 Bi-directional Emitter/Detector MicroLEDs

The commercial microLEDs used in this work are CREE DA1000 and CREE DA850 LEDs. The unique feature of these microLEDs are preformed AuSn solder bumps for eutectic die attach. This allows the microLEDs to be soldered to a substrate or circuit by aligning and heating the chips without the need to place solder on the bond pads. The DA 1000 LEDs have dimensions of 1 mm x 1 mm x 335 $\mu\text{m}$ . The DA 850 LEDs have dimensions of 850  $\mu\text{m}$  x 850  $\mu\text{m}$  x 335  $\mu\text{m}$ .

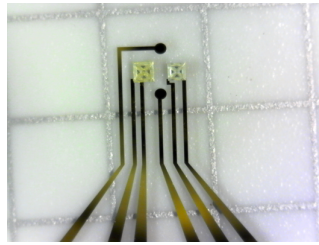


Figure 4.1: Photograph of the microLEDs soldered onto a glass substrate with a Cr/Au circuit. DA1000 LED (left) is 1 mm in length. DA 850 (right) is 850  $\mu\text{m}$  in length.

The microLEDs are used as both the emitter and detector for performing ORIS measurements. According to the Mims effect, LEDs are able to convert incoming light of equal or shorter wavelengths than the emission wavelength into photocurrent, making them effectively low-pass photodiodes.[32, 33] Thus, an array of microLEDs can be multiplexed as both emitters and detectors. For this work, blue and green microLEDs with emission wavelengths of 450 nm and 530 nm, respectively, were used. Figure 4.2 shows that the responsivity of the microLED acting as a photodiode drops significantly at wavelengths above the LED's emission wavelength. The overall performance of the microLEDs operating in photodiode mode (zero electrical bias) is presented in Table 4.1.

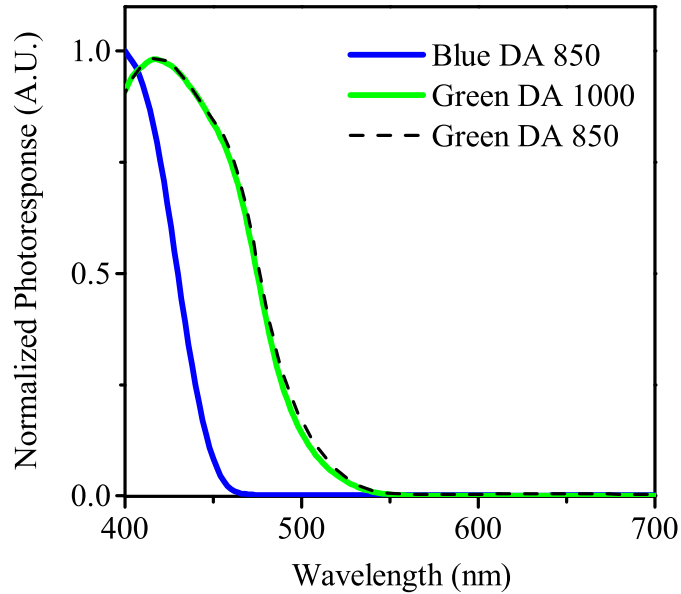


Figure 4.2: Spectral response of the microLEDs

	Emission wave- length	FWHM	Responsivity to blue microLED	Responsivity to green microLED	Responsivity to 555nm centered QD emission
Blue microLED	450 nm	30 nm	0.022 A/W	N/A	N/A
Green microLED	530 nm	28 nm	0.184 A/W	0.0060 A/W	0.0052 A/W

Table 4.1: Responsivity of microLEDs in photodiode mode to 3 different light emissions used in the ORIS device.

## 4.2 Device Fabrication

The microLEDs are soldered to a flexible polyimide substrate (Dupont Polyimide Kapton PV9103). Polyimide is an ideal flexible substrate that can withstand the wet chemical etching processes for forming the circuitry as well as the thermal processes for reflowing the microLEDs. The entire fabrication process is shown in Figure 4.3. First Cr/Au circuitry is thermally evaporated (at pressures on the order of  $1 \times 10^{-6}$  Torr) onto clean polyimide which is adhered to a glass carrier, and the Au/Cr layers are photolithographically patterned. Flux is applied to the bond pads and the microLEDs are aligned onto the bond pads. The whole device is then placed in a IR reflowed oven and thermally reflowed with a peak temperature of 280 C. After the microLEDs have been reflowed, poly(methyl methacrylate) (PMMA) photoresist is deposited directly on top of the microLEDs with a pneumatic printer and annealed at 100 C to harden the PMMA and remove solvents. The PMMA resist serves to relieve strain on the contacts of the microLEDs during flexing.[63] Heat seal connector is used to contact the devices by hot bar bonding, and finally, parylene-c is blanket deposited over the whole device to form a biocompatible encapsulation and interface. The completed devices are then delaminated from the glass carriers. The completed devices are shown in Figure 4.4.

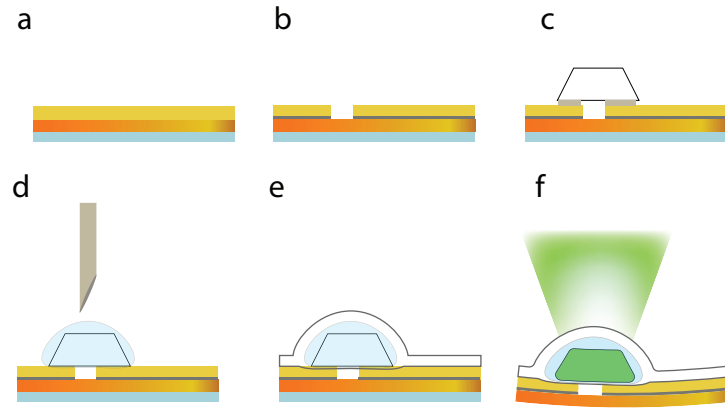


Figure 4.3: Fabrication steps for the microLED ORIS sensor. a) 40 nm Cr and then 150 nm Au are thermally evaporated onto a 25  $\mu\text{m}$  thick, clean polyimide sheet on a glass carrier. b) The circuit and bond pads are patterned via photolithography and wet etching. c) Flux is applied to the bond pads and the microLEDs are placed on the bond pads. The microLEDs are reflowed in an infrared reflow oven at 280 C. d) PMMA resist is deposited over the bonded microLEDs using a pneumatic printer. The devices are annealed at 100 C for 90 minutes to harden the PMMA resist and remove the solvent. e) Parylene-C is blanket-coated over the entire device after contacting the devices hot bar bonding. f) The completed device is delaminated from the glass carrier.

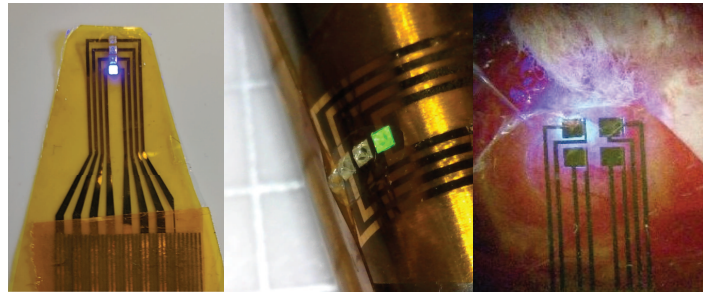


Figure 4.4: Photographs of the ORIS devices in operation. Left: Completed ORIS device is shown with a blue microLED operating in emitter mode. Middle: ORIS device flexed around a rod with 1/2 inch diameter. A green microLED is shown operating at the same time. Right: MicroLED ORIS device attached to the surface of a rat's brain.



### 4.3 In-Vivo Measurement of CBV and Seizure Detection

MicroLED-based ORIS devices with a  $850\text{ }\mu\text{m}$  blue microLED emitter and a 1 mm green microLED detector spaced 1.5 mm apart are attached to the surface of a rat's brain for *in vivo* measurement of CBV (Figure 4.4). In the same manner described in the previous chapter, the rat is anaesthetized and the brain is surgically exposed for attachment of the ORIS device. A needle electrode measuring the local field potential (LFP) as a reference signal for neural activity is implanted near the ORIS device's site of attachment. A microLED in emitter mode is powered, while an adjacent microLED is operated in photodiode mode, measuring the reflected optical signal.

Baseline variations of cerebral blood volume (CBV) are measured, including hemodynamic changes due to the heartbeat, respiration, and slow sinusoidal harmonic oscillations in the brain of the animal (Figure 4.5). The dominant element in the baseline signal is the heartbeat which is shown having a frequency of 6 Hz.

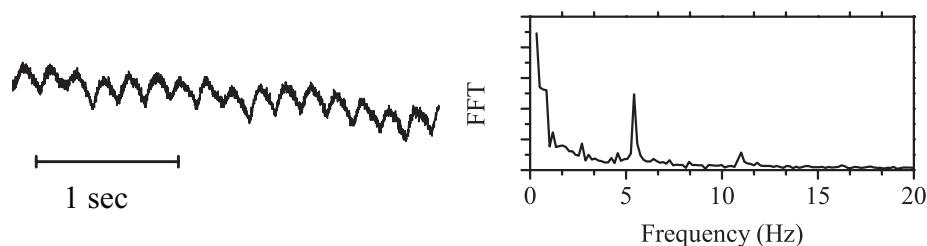


Figure 4.5: Baseline Measurements of CBV by the microLED ORIS device. Left: ORIS measurement of baseline CBV signals. Variations in the ORIS signal are due to changes in CBV. Right: FFT of the baseline CBV signals.

After injection of 4AP to induce seizures in the brain, the ORIS device records changes in the reflected optical signal due to the hemodynamic response to seizures. Seizure detection using a green microLED in photodiode mode is shown in Figure 4.6. A device with the same layout but using two blue  $850\text{ }\mu\text{m}$  microLEDs is also used to detect seizure (Figure 4.7).

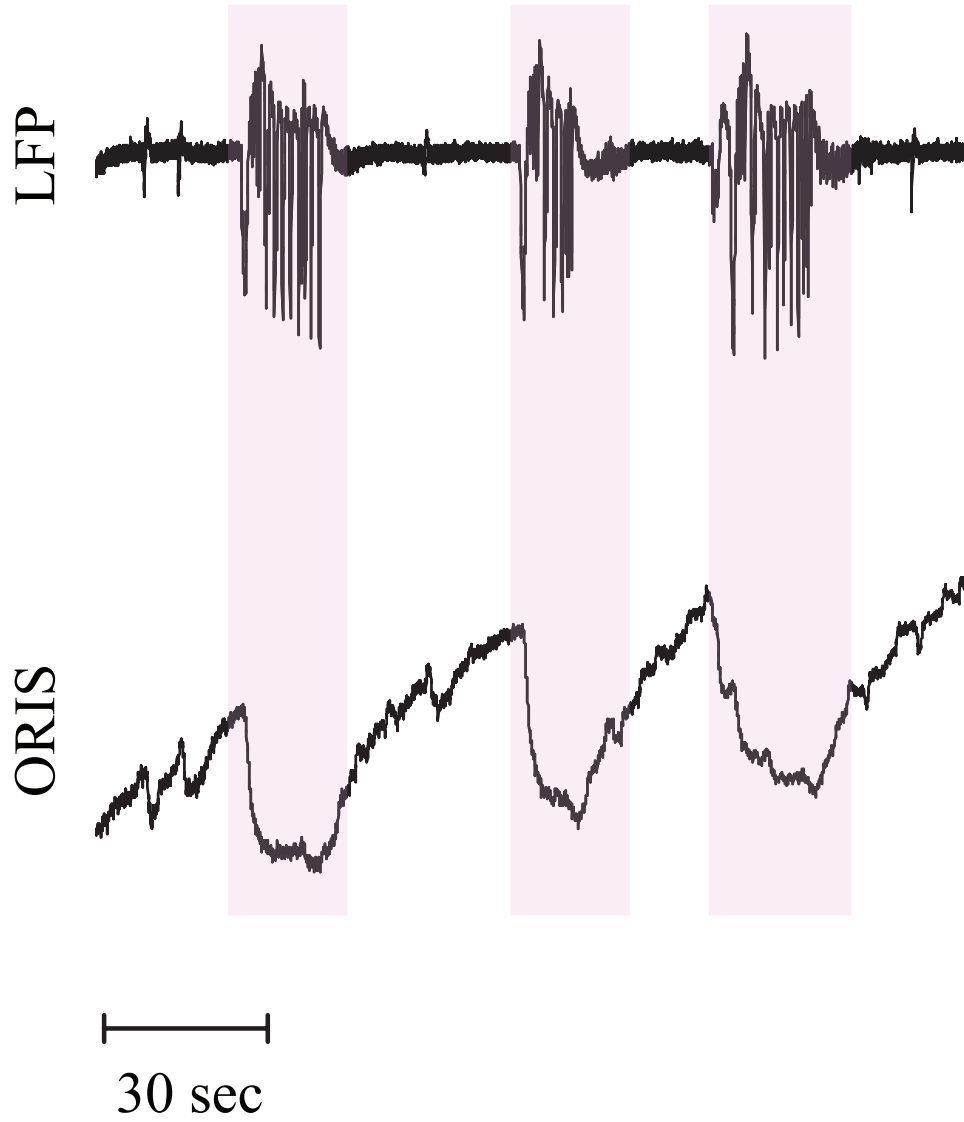


Figure 4.6: *In vivo* seizure detection using blue-to-green microLED ORIS device. Duration of seizures are shaded in pink. Seizures are detected with a signal-to-noise ratio greater than 33 dB. SNR is determined by comparing the root mean square amplitude of the baseline oscillations to the excursion in amplitude during seizure events.

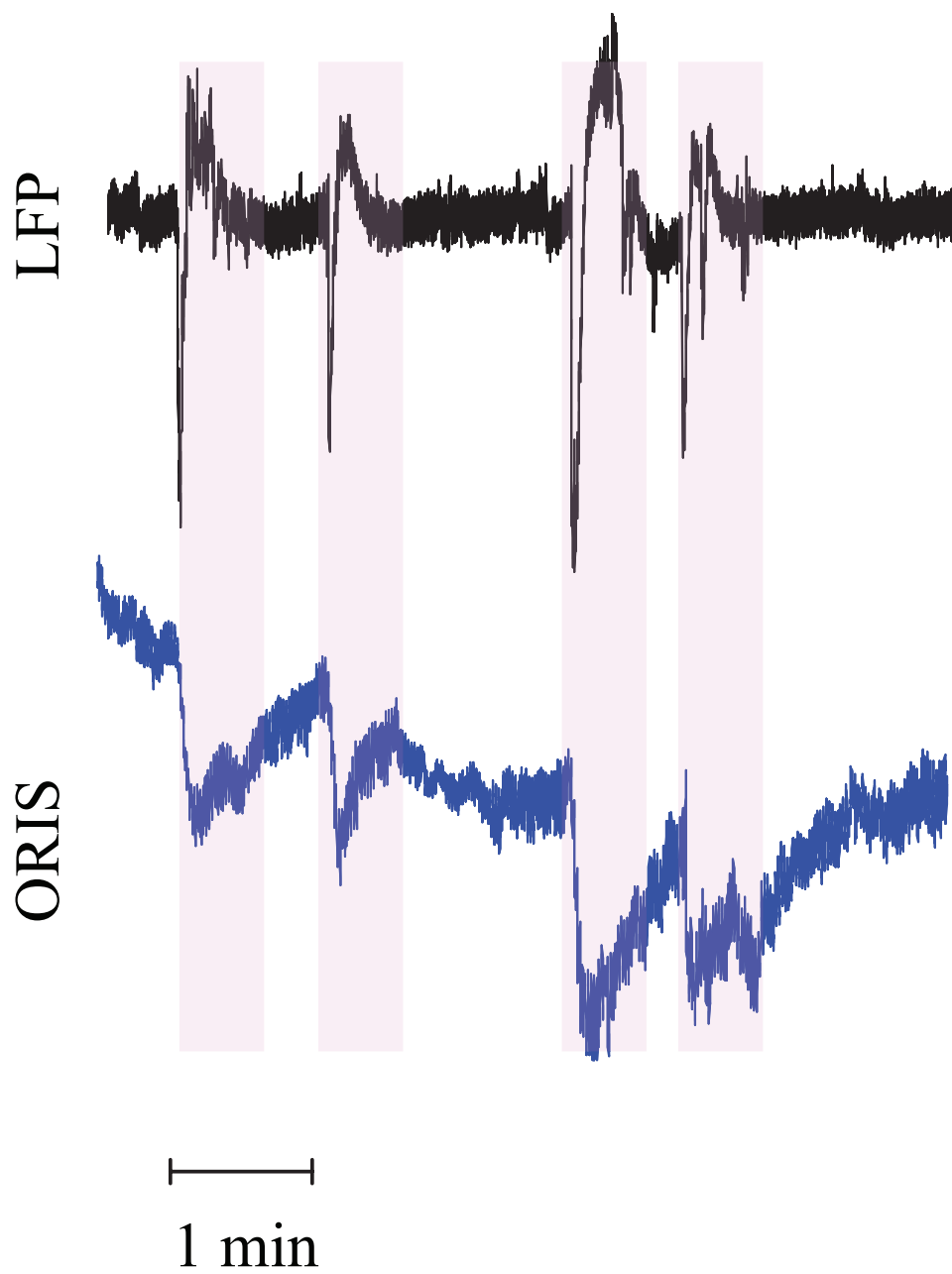


Figure 4.7: *In vivo* seizure detection using blue-to-blue microLED ORIS device. Duration of seizures are shaded in pink. High SNR of seizure detection is achieved despite the lower responsivity of the blue microLEDs.

At the onset of each seizure, blood rushes to the site of the seizure in response to the increased neural activity resulting in a dip in the ORIS signal collected by the microLED in photodiode mode. As the neural activity returns to the baseline, the CBV levels decrease and the ORIS signal relaxes towards the baseline level. The blue-to-green ORIS device was able to detect seizures with a signal-to-noise ratio (SNR) greater than 33 dB. The blue-to-blue device has a similarly high SNR greater than 18 dB, despite the lower responsivity of the blue microLEDs in photodiode mode since the heartbeat signal presents the largest source of noise for seizure detection and the amplitude of heartbeat oscillations decreases with the lower responsivity of the blue microLED detectors.

Another device with 4 microLED elements configured in a linear array is attached to a rat's brain for detecting localized changes in CBV during seizures. The layout for this device is shown in Figure 4.8. 2 green microLEDs, PD1 and PD2, operate in photodiode mode measuring the reflected ORIS signal, while 2 blue microLEDs operate in emitter mode. PD1, which is closer to the focus of the seizure, observes an increase in CBV and relaxation back to the baseline with each seizure that occurs. PD2 detects different changes in CBV at the site of attachment. The recorded CBV changes with varying amplitude and duration due to dynamic metabolic demands of the brain during seizures of different severity. This localized hemodynamic response, shown in Figure 4.9, is consistent with earlier observed measurements of CBV.[29] This demonstration of localization of hemodynamic changes during seizure events shows the potential of the microLED ORIS device to be used for large area, high resolution imaging of neural activity. By using a full 2D array of microLEDs in this device architecture, spatial resolutions on the order of 1 mm x 1 mm are possible. Further, by switching to smaller microLED elements, spatial resolutions approaching those achieved with CCD cameras ( $< 200 \mu\text{m}$ ) may be possible. This kind of performance at high resolutions would be comparable to advanced ECoG arrays with sub-millimeter inter-electrode spacing.[20, 21]

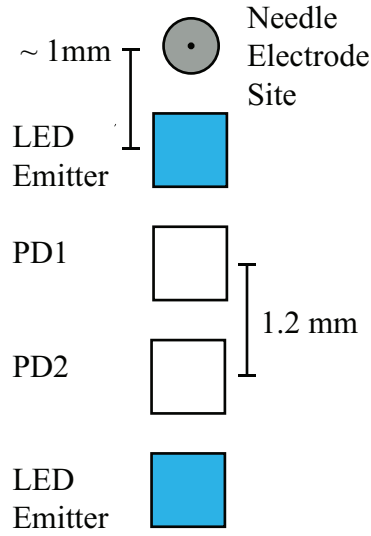


Figure 4.8: Layout of the linear array device. The two microLEDs in photodiode mode, PD1 and PD2, are attached roughly 2 mm and 3.2 mm away from the focus of the seizure which occurs at the site of 4AP injection.

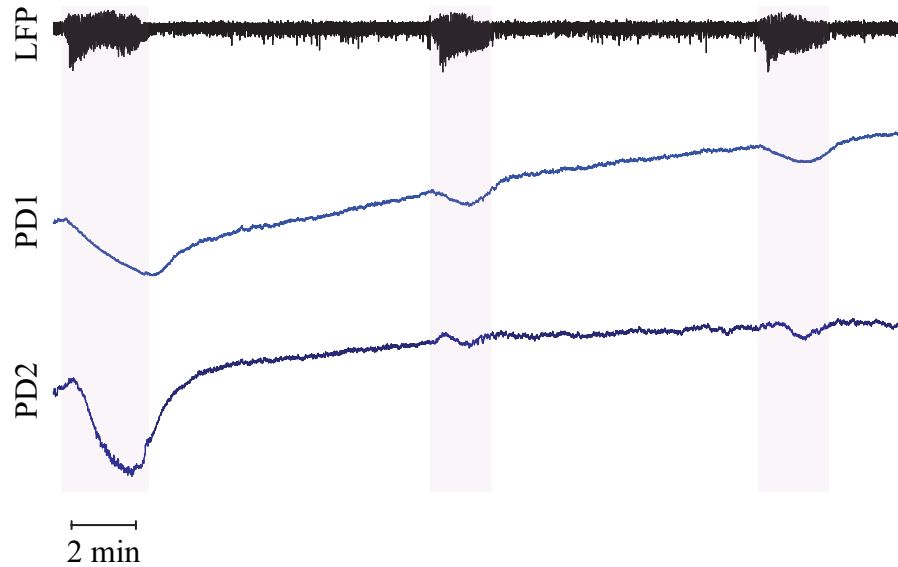


Figure 4.9: Localized measurements of CBV using a linear array of microLEDs. The microLED detector labeled “PD2” is 1.2 mm further away from the focus of the seizure than PD1. The duration of seizures at the epileptic focus are highlighted in pink. Notch filtering to remove the out of band signals is used to improve the detection of seizures.

## 4.4 MicroLED ORIS Sensor with Quantum Dot Optical Down-Conversion Coating

In order to select emission wavelengths outside of the discrete wavelengths available for commercial microLEDs, quantum dot (QD) composite coatings are applied to microLEDs via pneumatic printing. CdS/CdSe/CdS core shell quantum dots are suspended in toluene at a concentration of 20 mg/mL. The QD:PMMA composite is prepared by mixing an equal weight of the QD (in toluene) solution with 950 A6 PMMA photoresist (MicroChem). The mixture is heated at 70 C for 45 minutes while being stirred with a magnetic stir bar to increase the viscosity. The fabrication of the devices with the QD coatings is identical to the one described above (Figure 4.3), with the QD:PMMA composite replacing PMMA photoresist. By utilizing the pneumatic printing technique described in Yang et al.,[90] the QD coatings can be applied to individual microLEDs without affecting adjacent elements, allowing for the use of multiple emission wavelengths using only blue microLEDs. Photographs of the printing set up and microLEDs with applied QD coatings is shown in Figure 4.10.

Figure 4.11 shows the emission spectra for the microLEDs directly after the QD coatings have been applied. Some of the blue backlight is emitted out due to both light leaking through the QD coating and back-reflections from the substrate, but the QD coatings are able to perform well as color conversion layers with the addition of a color filter for removing the blue backlight. . For the amber QD coating, 86.2% of the emitted light is down-converted. For the red QD coating 95.5% of the emitted light is down-converted. For the green QD coating 89.5% of the emitted light is down-converted. Conversion percentage is calculated by comparing the integral of light intensity in the 500 nm to 750 nm range to the integral of light intensity over the entire spectral range.

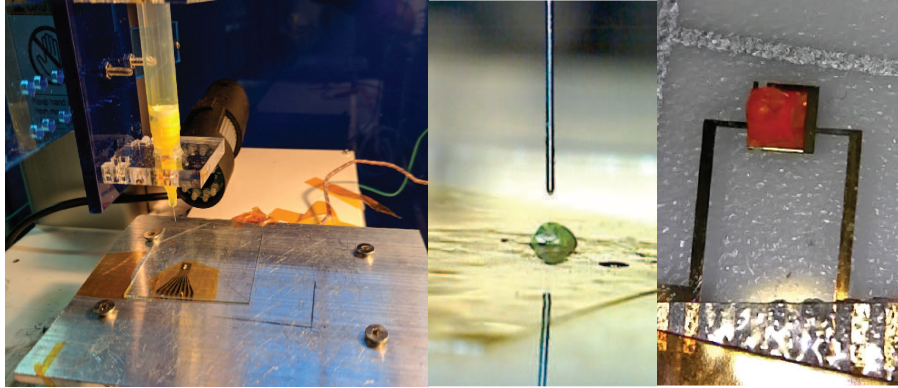


Figure 4.10: Pneumatic printing QD optical down-conversion coatings. Photographs left to right: pneumatic printing set up, green QD coating being applied to a microLED, microLED with applied amber QD coating.

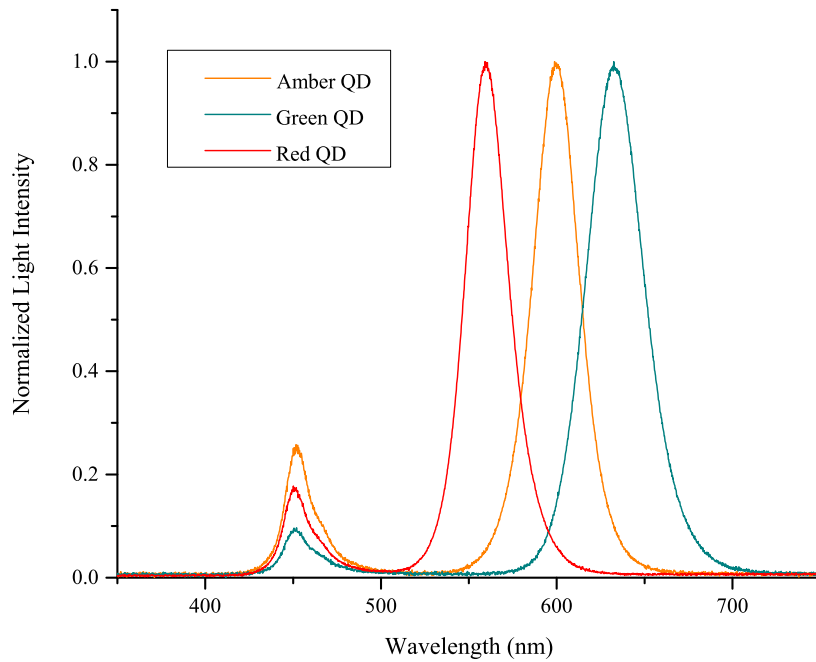


Figure 4.11: Emission spectra for MicroLED coatings without filtering. The blue component of the emitted light is from microLED backlight that has not been absorbed or has been back-reflected from the substrate.

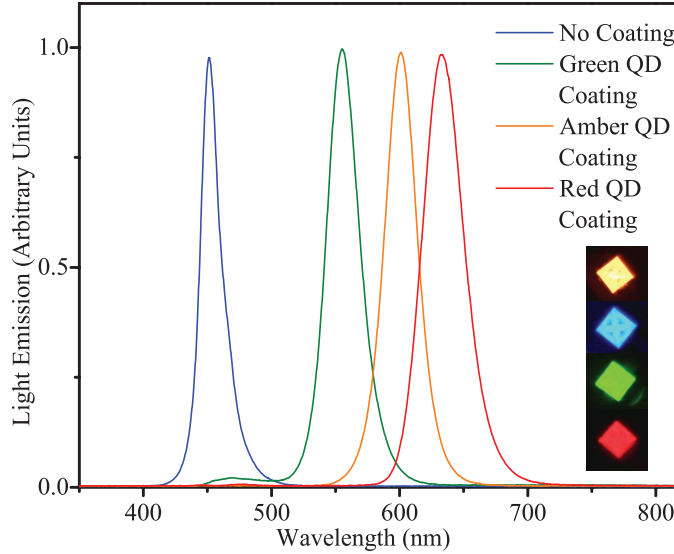


Figure 4.12: Emission spectra of optical QD down-conversion of blue microLED backlight. Inset: photographs of the microLEDs with QD coatings shown operating. Roscolux gel filters and polyimide sheets are used to filter any blue emission not absorbed by the QDs.

The emission spectra of QD coatings with the addition of color filtering are shown in Figure 4.12. Roscolux 4690 and 2003 gel filters are used for the red and amber QD coatings, while polyimide sheets are used for the green QD coatings to filter out any blue backlight that is not absorbed by the QDs. Using QD coatings such as the three variants shown in this work enables the control of emission wavelength within a few nm with a narrow ( $<50$  nm FWHM) spectrum. The hardened composites also provide a dual function of strain relief for the contacts. [63]

An implantable ORIS device with a green QD down-conversion is attached to the surface of a rat's brain for ORIS measurement of seizure events. The green QD coating has a peak emission wavelength of 555 nm, and an adjacent green microLED records the reflected ORIS signal. The device is able to detect changes in CBV due to the hemodynamic response of the brain during seizures, similar to the other devices described in this chapter (Figure 4.13)



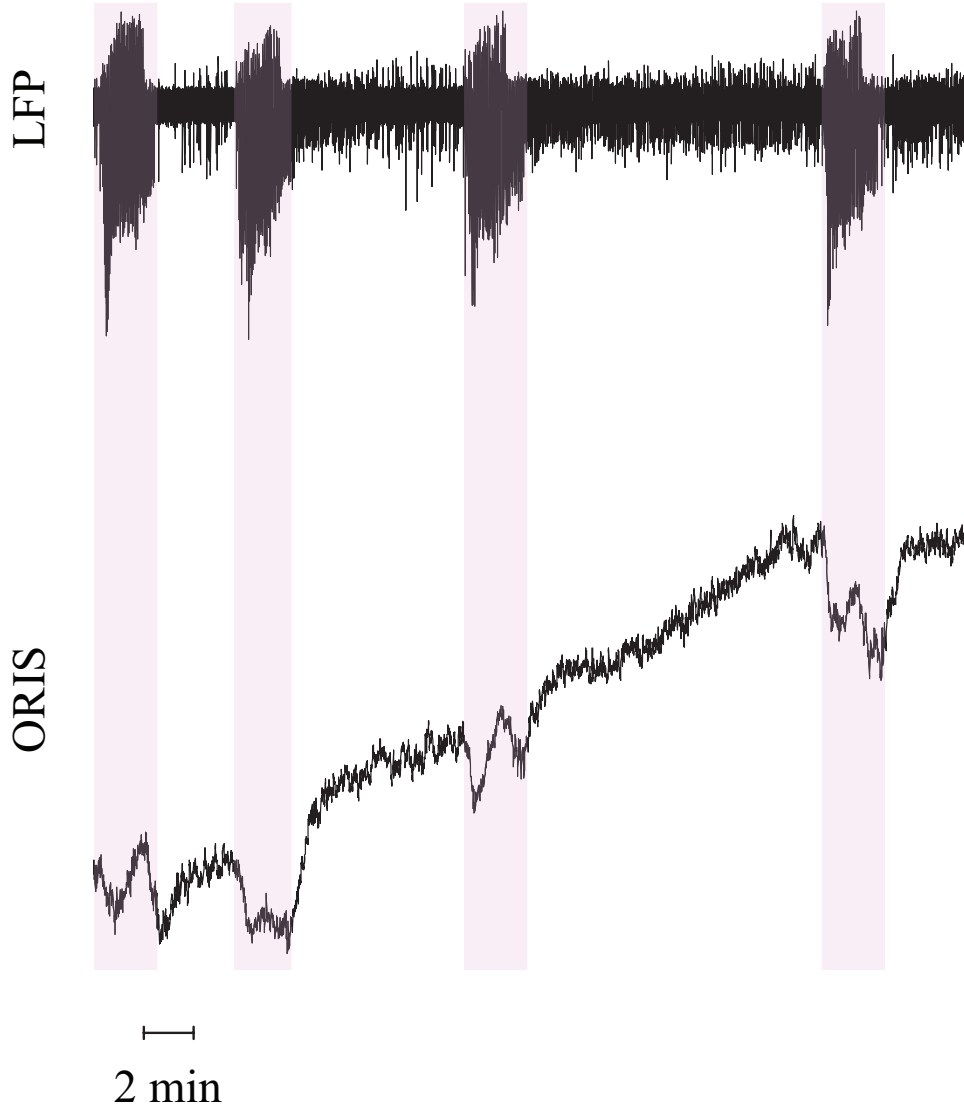


Figure 4.13: Seizure detection using a microLED ORIS device with green QD down-conversion coating. Duration of seizures is highlighted in pink. Notch filtering to remove the out-of-band signals is used to improve the detection of seizures.

The ability to select specific wavelengths for measurement expands the applicability of the device to other isosbestic points in the hemoglobin absorbance spectrum as well as other biomedical fields. Various isosbestic wavelengths are preferred for clinical, diagnostic measurement [91] and having the ability to target a desired isosbestic point without having to drastically alter the device architecture and materials makes the microLED ORIS device

a versatile choice for clinical and biomedical research applications. Additionally, applications such as pulse-oximetry which requires simultaneous measurement of non-isosbestic points and the measurement of fetal hemoglobin, which has a different absorbance spectrum than adult hemoglobin, may benefit from this device architecture.[92] An implantable ORIS monitoring device can even be configured to provide optogenetic-triggered inhibition of seizures.[93]

## 4.5 Chapter Summary

An ORIS device comprised of bi-directional microLED emitter/detector pairs integrated on a flexible polyimide substrate are presented. Localization of hemodynamic response to seizures is reported as well as the use of QD optical down-conversion coatings. The device presented in this chapter has potential for being a next-generation alternative to clinical ECoG measurement for the diagnosis and treatment of epilepsy, as well as other applications.

## Chapter 5

# Conclusion

Wearable and implantable sensors have great promise for enabling the next generation of healthcare diagnostics and treatment methods. Although there has been great excitement over the benefits of computational analysis in personalized healthcare, improvements in hardware and sensing applications are necessary for extracting relevant, practical data. This is especially true for surgeons and researchers studying epilepsy. Improvements over current clinical methods for neuronal mapping have the potential to drastically improve the success of surgical treatments that involve resection of brain matter. Implantable sensors performing ORIS measurements of CBV and other factors in the brain have the potential to provide an alternative method for high spatiotemporal resolution of neuronal activity in clinical settings.

The work presented here has advanced the development of an implantable optical sensor for performing ORIS mapping in the brain. These advances include: the design, fabrication, and testing of implantable ORIS devices using organic LEDs, organic photodetectors, and microLEDs on a variety of flexible substrates. The demonstrated organics based devices like the one described in Chapter 3 may be useful for acute clinical measurements and applications outside of ORIS measurement which require extreme levels of flexibility and low device thickness. The demonstration of a flexible microLED-based sensor is a candidate for long-term, chronic measurements of CBV and neuronal activity, thanks to its high optical performance and long operational lifetimes. Moreover, the localization of seizure activity in the brain using an arrayed microLED ORIS sensor is a crucial step in achieving full 2D

mapping of neuronal activity with an implantable ORIS sensor. Finally, the application of quantum dots to the flexible microLED sensor has extended the functionality of such devices, by increasing the effective range of available emission wavelengths produced by commercial microLEDs.

Much work remains in developing an implantable ORIS system capable of high spatiotemporal, 2D mapping of neuronal activity. In addition to continued advancement of the hardware, combining the sensors developed in this work with advanced computational and analysis methods may provide even higher fidelity sensing and open the devices to new applications. With continued development, an “optical pacemaker” for the brain may eventually be achieved. Such a device would couple the continuous monitoring of neuronal activity the ability to locally administer treatments such as optogenetic-triggered neuronal inhibition, drug delivery, or electric stimulation. This would mark a true leap in the diagnosis and treatment of neurological diseases such as epilepsy.

# Publications and Presentations

1. Christopher Choi, Aida R. Colón-Berrios, Leslie S. Hamachi, Jonathan S. Owen, Theodore H. Schwartz, Hongtao Ma, and Ioannis Kymissis. "Localizing Seizure Activity in the Brain Using Implantable Micro-LEDs with Quantum Dot Downconversion." *Advanced Materials Technologies* (2018): 1700366.
2. Brigitte Holzer, Johannes Binting, Daniel Lumpi, Christopher Choi, Youngwan Kim, Berthold Stöger, Christian Hametner et al. "Color Fine-Tuning of Optical Materials Through Rational Design." *ChemPhysChem* 18, no. 5 (2017): 549-563.
3. Youngwan Kim, Christopher Choi, En-Chen Chen, Andy G. S. Daniel, Amrita Masurkar, Theodore H. Schwartz, Hongtao Ma, Andreas H. Hielscher and Ioannis Kymissis. (2016, May). "Ultra-thin, Flexible, and Implantable Optical Sensor." Poster presented at Display Week 2016, Innovation Zone. San Francisco, CA.
4. Youngwan Kim, Christopher Choi, En-Chen Chen, Andy G. S. Daniel, Amrita Masurkar, Theodore H. Schwartz, Hongtao Ma, and Ioannis Kymissis. (2016, April). "An Ultra Thin Implantable System for Cerebral Blood Volume Monitoring Using Flexible OLED and OPD." Presented at the 25th annual Connecticut Microelectronics and Optoelectronics Consortium. Storrs, CT.
5. Youngwan Kim, Christopher Choi, En-Chen Chen, Andy GS Daniel, Amrita Masurkar, Theodore H. Schwartz, Hongtao Ma, and Ioannis Kymissis. "An ultra thin implantable system for cerebral blood volume monitoring using flexible OLED and OPD." In *Electron Devices Meeting (IEDM), 2015 IEEE International*, pp. 29-6. IEEE, 2015.

# Bibliography

- [1] Annalisa Bonfiglio, Ileana Manunza, Alessandra Caboni, Werther Cambarau, and Massimo Barbaro. Organic field-effect based sensors for body parameters monitoring. *Proc. SPIE Photon*, pages 665904–1, 2007.
- [2] Claire M Lochner, Yasser Khan, Adrien Pierre, and Ana C Arias. All-organic optoelectronic sensor for pulse oximetry. *Nature communications*, 5:5745, 2014.
- [3] Hyunsu Cho, Changhun Yun, Jae-Woo Park, and Seunghyup Yoo. Highly flexible organic light-emitting diodes based on zns/ag/wo 3 multilayer transparent electrodes. *Organic Electronics*, 10(6):1163–1169, 2009.
- [4] Xiaochen Ren, Ke Pei, Boyu Peng, Zhichao Zhang, Zongrong Wang, Xinyu Wang, and Paddy KL Chan. A low-operating-power and flexible active-matrix organic-transistor temperature-sensor array. *Advanced Materials*, 28(24):4832–4838, 2016.
- [5] Tomoyuki Yokota, Peter Zalar, Martin Kaltenbrunner, Hiroaki Jinno, Naoji Matsuhisa, Hiroki Kitanosako, Yutaro Tachibana, Wakako Yukita, Mari Koizumi, and Takao Someya. Ultraflexible organic photonic skin. *Science advances*, 2(4):e1501856, 2016.
- [6] Ingrid Graz, Markus Krause, Simona Bauer-Gogonea, Siegfried Bauer, Stephanie P Lacour, Bernd Ploss, Martin Zirkel, Barbara Stadlober, and Sigurd Wagner. Flexible active-matrix cells with selectively poled bifunctional polymer-ceramic nanocomposite for pressure and temperature sensing skin. *Journal of Applied Physics*, 106(3):034503, 2009.
- [7] Kyriaki Manoli, Gerardo Palazzo, Eleonora Macchia, Amber Tiwari, Cinzia Di Franco,

- Gaetano Scamarcio, Pietro Favia, Antonia Mallardi, and Luisa Torsi. Electrolyte gated tft biosensors based on the donnan's capacitance of anchored biomolecules. In *Organic Sensors and Bioelectronics X*, volume 10364, page 103640J. International Society for Optics and Photonics, 2017.
- [8] Ileana Manunza, Emanuele Orgiu, Alessandra Caboni, Massimo Barbaro, and Annalisa Bonfiglio. Producing smart sensing films by means of organic field effect transistors. In *Engineering in Medicine and Biology Society, 2006. EMBS'06. 28th Annual International Conference of the IEEE*, pages 4344–4346. IEEE, 2006.
- [9] Yilin Song, Jonathan Viventi, and Yao Wang. Unsupervised learning of spike patterns for seizure detection and wavefront estimation of high resolution micro electrocorticographic ( $\mu$  ecog) data. *arXiv preprint arXiv:1706.00780*, 2017.
- [10] B Samanta and C Nataraj. Automated diagnosis of cardiac state in healthcare systems using computational intelligence. *International Journal of Services Operations and Informatics*, 3(2):162–177, 2008.
- [11] Monica Tentori and Jesus Favela. Activity-aware computing for healthcare. *IEEE Pervasive Computing*, 7(2), 2008.
- [12] Epilepsy fact sheet. <http://www.who.int/mediacentre/factsheets/fs999/en/>, 02 2017. World Health Organization Website.
- [13] Marvin M Goldenberg. Overview of drugs used for epilepsy and seizures: etiology, diagnosis, and treatment. *Pharmacy and Therapeutics*, 35(7):392, 2010.
- [14] Edward B Bromfield, José E Cavazos, and Joseph I Sirven. *An introduction to epilepsy*. American Epilepsy Society, 2006.
- [15] Daniel H. Lowenstein. *Seizures and Epilepsy*, chapter 369. The McGraw-Hill Companies, New York, NY, 2012.
- [16] Blausen Staff. Medical gallery of blausen medical 2014. *WikiJournal of Medicine*, 1(2):10, 2014.

- [17] Robert S Fisher, Barbara G Vickrey, Patricia Gibson, Bruce Hermann, Patricia Penovich, Ann Scherer, and Steven Walker. The impact of epilepsy from the patient's perspective i. descriptions and subjective perceptions. *Epilepsy research*, 41(1):39–51, 2000.
- [18] H Lüders, I Awad, R Burgess, E Wyllie, and P Van Ness. Subdural electrodes in the presurgical evaluation for surgery of epilepsy. *Epilepsy Research. Supplement*, 5:147–156, 1992.
- [19] Taro Kaiju, Keiichi Doi, Masashi Yokota, Kei Watanabe, Masato Inoue, Hiroshi Ando, Kazutaka Takahashi, Fumiaki Yoshida, Masayuki Hirata, and Takafumi Suzuki. High spatiotemporal resolution ecog recording of somatosensory evoked potentials with flexible micro-electrode arrays. *Frontiers in neural circuits*, 11, 2017.
- [20] Dion Khodagholy, Jennifer N Gelinas, Thomas Thesen, Werner Doyle, Orrin Devinsky, George G Malliaras, and György Buzsáki. Neurogrid: recording action potentials from the surface of the brain. *Nature neuroscience*, 18(2):310–315, 2015.
- [21] Dion Khodagholy, Jennifer N Gelinas, Zifang Zhao, Malcolm Yeh, Michael Long, Jeremy D Greenlee, Werner Doyle, Orrin Devinsky, and György Buzsáki. Organic electronics for high-resolution electrocorticography of the human brain. *Science Advances*, 2(11):e1601027, 2016.
- [22] Subhas Chandra Mukhopadhyay. Wearable sensors for human activity monitoring: A review. *IEEE sensors journal*, 15(3):1321–1330, 2015.
- [23] Xudong Ji, Ho Yuen Lau, Xiaochen Ren, Boyu Peng, Peng Zhai, Shien-Ping Feng, and Paddy KL Chan. Bioelectronics: Highly sensitive metabolite biosensor based on organic electrochemical transistor integrated with microfluidic channel and poly (n-vinyl-2-pyrrolidone)-capped platinum nanoparticles (adv. mater. technol. 5/2016). *Advanced Materials Technologies*, 1(5), 2016.
- [24] Danilo Pani, Alessia Dessì, Jose F Saenz-Cogollo, Gianluca Barabino, Beatrice Fraboni, and Annalisa Bonfiglio. Fully textile, pedot: Pss based electrodes for wearable ecg



- monitoring systems. *IEEE Transactions on Biomedical Engineering*, 63(3):540–549, 2016.
- [25] TAGA Bonhoeffer. Optical imaging based on intrinsic signals the methodology. *Brain mapping: The methods*, pages 55–97, 1996.
- [26] Theodore H Schwartz. The application of optical recording of intrinsic signals to simultaneously acquire functional, pathological and localizing information and its potential role in neurosurgery. *Stereotactic and functional neurosurgery*, 83(1):36–44, 2005.
- [27] Minah Suh, Sonya Bahar, Ashesh D Mehta, and Theodore H Schwartz. Temporal dependence in uncoupling of blood volume and oxygenation during interictal epileptiform events in rat neocortex. *Journal of Neuroscience*, 25(1):68–77, 2005.
- [28] Minah Suh, Sonya Bahar, Ashesh D Mehta, and Theodore H Schwartz. Blood volume and hemoglobin oxygenation response following electrical stimulation of human cortex. *Neuroimage*, 31(1):66–75, 2006.
- [29] Minah Suh, Hongtao Ma, Mingrui Zhao, Saadat Sharif, and Theodore H Schwartz. Neurovascular coupling and oximetry during epileptic events. *Molecular neurobiology*, 33(3):181–197, 2006.
- [30] Scott Prahl et al. Optical absorption of hemoglobin. <http://omlc.org/spectra/hemoglobin/>, 1999.
- [31] Marshall P Cox, Hongtao Ma, Matthias E Bahlke, Jonathan H Beck, Theodore H Schwartz, and Ioannis Kymissis. Led-based optical device for chronic in vivo cerebral blood volume measurement. *IEEE transactions on electron devices*, 57(1):174–177, 2010.
- [32] Forrest M Mims. *Siliconconnections: Coming of age in the electronic era*. McGraw-Hill Companies, 1986.
- [33] Forrest M Mims. *LED Circuits and Projects*. Howard W. Sams and Co., Inc, 1979.

- [34] E Menard, Ralph G Nuzzo, and John A Rogers. Bendable single crystal silicon thin film transistors formed by printing on plastic substrates. *Applied Physics Letters*, 86(9):093507, 2005.
- [35] John A Rogers, Takao Someya, and Yonggang Huang. Materials and mechanics for stretchable electronics. *Science*, 327(5973):1603–1607, 2010.
- [36] Ioannis Kyriakidis. *Organic Field Effect Transistors: Theory, Fabrication and Characterization*. Springer Science & Business Media, 2008.
- [37] H Mu, W Li, R Jones, A Steckl, and D Klotzkin. A comparative study of electrode effects on the electrical and luminescent characteristics of alq 3/tpd oled: Improvements due to conductive polymer (pedot) anode. *Journal of Luminescence*, 126(1):225–229, 2007.
- [38] Takatoshi Tsujimura. *OLED display fundamentals and applications*. John Wiley & Sons, 2017.
- [39] MAa Baldo, Sb Lamansky, PEc Burrows, MEb Thompson, and SRl Forrest. Very high-efficiency green organic light-emitting devices based on electrophosphorescence. *Applied Physics Letters*, 75(1):4–6, 1999.
- [40] Stefan Kappaun, Christian Slugovc, and Emil JW List. Phosphorescent organic light-emitting devices: Working principle and iridium based emitter materials. *International journal of molecular sciences*, 9(8):1527–1547, 2008.
- [41] Hoang-Yan Lin, Yu-Hsuan Ho, Juin-Haw Lee, Kuan-Yu Chen, Jheng-Hao Fang, Sheng-Chih Hsu, Mao-Kuo Wei, Hung-Yi Lin, Jen-Hui Tsai, and Tung-Chuan Wu. Patterned microlens array for efficiency improvement of small-pixelated organic light-emitting devices. *Optics express*, 16(15):11044–11051, 2008.
- [42] Hyun Soo Kim, Seong Il Moon, Dong Eui Hwang, Ki Won Jeong, Chang Kyo Kim, Dae-Gyu Moon, and Chinsoo Hong. Novel fabrication method of microlens arrays with high oled outcoupling efficiency. *Optics & Laser Technology*, 77:104–110, 2016.

- [43] Hany Aziz and Zoran D Popovic. Degradation phenomena in small-molecule organic light-emitting devices. *Chemistry of Materials*, 16(23):4522–4532, 2004.
- [44] PE Burrows, V Bulovic, SR Forrest, L Sl Sapochak, DM McCarty, and ME Thompson. Reliability and degradation of organic light emitting devices. *Applied Physics Letters*, 65(23):2922–2924, 1994.
- [45] Wei-Chun Lin, Wei-Ben Wang, Yu-Chin Lin, Bang-Ying Yu, Ying-Yu Chen, Mao-Feng Hsu, Jwo-Huei Jou, and Jing-Jong Shyue. Migration of small molecules during the degradation of organic light-emitting diodes. *Organic Electronics*, 10(4):581–586, 2009.
- [46] Qian Yang, Yuying Hao, Zhenguo Wang, Yunfei Li, Hua Wang, and Bingshe Xu. Double-emission-layer green phosphorescent oled based on lif-doped tpbi as electron transport layer for improving efficiency and operational lifetime. *Synthetic Metals*, 162(3):398–401, 2012.
- [47] A Ra Cho, Eun Hye Kim, Soo Young Park, and Lee Soon Park. Flexible oled encapsulated with gas barrier film and adhesive gasket. *Synthetic Metals*, 193:77–80, 2014.
- [48] Samuel P Subbarao, Matthias E Bahlke, and Ioannis Kymissis. Laboratory thin-film encapsulation of air-sensitive organic semiconductor devices. *IEEE Transactions on Electron Devices*, 57(1):153–156, 2010.
- [49] Jay S Lewis and Michael S Weaver. Thin-film permeation-barrier technology for flexible organic light-emitting devices. *IEEE Journal of selected topics in quantum electronics*, 10(1):45–57, 2004.
- [50] Jin-Seong Park, Heeyeop Chae, Ho Kyoong Chung, and Sang In Lee. Thin film encapsulation for flexible am-oled: a review. *Semiconductor science and technology*, 26(3):034001, 2011.
- [51] Ross D Jansen-van Vuuren, Ardalan Armin, Ajay K Pandey, Paul L Burn, and Paul Meredith. Organic photodiodes: the future of full color detection and image sensing. *Advanced Materials*, 28(24):4766–4802, 2016.

- [52] Gordon J Hedley, Alexander J Ward, Alexander Alekseev, Calvyn T Howells, Emiliano R Martins, Luis A Serrano, Graeme Cooke, Arvydas Ruseckas, and Ifor DW Samuel. Determining the optimum morphology in high-performance polymer-fullerene organic photovoltaic cells. *Nature communications*, 4:2867, 2013.
- [53] Kang-Jun Baeg, Maddalena Binda, Dario Natali, Mario Caironi, and Yong-Young Noh. Organic light detectors: photodiodes and phototransistors. *Advanced materials*, 25(31):4267–4295, 2013.
- [54] Sung Heum Park, Anshuman Roy, Serge Beaupré, Shinuk Cho, Nelson Coates, Ji Sun Moon, Daniel Moses, Mario Leclerc, Kwanghee Lee, and Alan J Heeger. Bulk heterojunction solar cells with internal quantum efficiency approaching 100%. *Nature photonics*, 3(5):297–302, 2009.
- [55] Gang Yu, Jun Gao, Jan C Hummelen, Fred Wudl, and Alan J Heeger. Polymer photovoltaic cells: Enhanced efficiencies via a network of internal donor-acceptor heterojunctions. *Science*, 270(5243):1789, 1995.
- [56] Szuheng Ho, Shuyi Liu, Ying Chen, and Franky So. Review of recent progress in multilayer solution-processed organic light-emitting diodes. *Journal of Photonics for Energy*, 5(1):057611–057611, 2015.
- [57] Claire M Lochner, Yasser Khan, Adrien Pierre, and Ana C Arias. All-organic optoelectronic sensor for pulse oximetry. *Nature communications*, 5:5745, 2014.
- [58] Jason R Wojciechowski, Lisa C Shriver-Lake, Mariko Y Yamaguchi, Erwin Fullreder, Roland Pieler, Martin Schamesberger, Christoph Winder, Hans Jürgen Prall, Max Sonnleitner, and Frances S Ligler. Organic photodiodes for biosensor miniaturization. *Analytical chemistry*, 81(9):3455–3461, 2009.
- [59] Eeshita Manna, Teng Xiao, Joseph Shinar, and Ruth Shinar. Organic photodetectors in analytical applications. *Electronics*, 4(3):688–722, 2015.
- [60] I Ozden, M Diagne, AV Nurmikko, J Han, and T Takeuchi. A matrix addressable 1024

- element blue light emitting ingan qw diode array. *physica status solidi (a)*, 188(1):139–142, 2001.
- [61] François Olivier, Anis Daami, Ludovic Dupré, Franck Henry, Bernard Aventurier, and François Templier. 25-4: Investigation and improvement of 10 $\mu$ m pixel-pitch gan-based micro-led arrays with very high brightness. In *SID Symposium Digest of Technical Papers*, volume 48, pages 353–356. Wiley Online Library, 2017.
- [62] HX Jiang and JY Lin. Nitride micro-leds and beyond-a decade progress review. *Optics express*, 21(103):A475–A484, 2013.
- [63] Junghwan Byun, Byeongmoon Lee, Eunho Oh, Hyunjong Kim, Sangwoo Kim, Seunghwan Lee, and Yongtaek Hong. Fully printable, strain-engineered electronic wrap for customizable soft electronics. *Scientific Reports*, 7:45328, 2017.
- [64] V Poher, N Grossman, GT Kennedy, K Nikolic, HX Zhang, Z Gong, EM Drakakis, E Gu, MD Dawson, PMW French, et al. Micro-led arrays: a tool for two-dimensional neuron stimulation. *Journal of Physics D: Applied Physics*, 41(9):094014, 2008.
- [65] Kate L Montgomery, Alexander J Yeh, John S Ho, Vivien Tsao, Shrivats Mohan Iyer, Logan Grosenick, Emily A Ferenczi, Yuji Tanabe, Karl Deisseroth, Scott L Delp, et al. Wirelessly powered, fully internal optogenetics for brain, spinal and peripheral circuits in mice. *Nature methods*, 12(10):969–974, 2015.
- [66] Christian Gößler, Colin Bierbrauer, Rüdiger Moser, Michael Kunzer, Katarzyna Holc, Wilfried Pletschen, Klaus Köhler, Joachim Wagner, Michael Schwaerzle, Patrick Ruther, et al. Gan-based micro-led arrays on flexible substrates for optical cochlear implants. *Journal of Physics D: Applied Physics*, 47(20):205401, 2014.
- [67] Sowmya Venkataramani, Kristina M Davitt, Jiayi Zhang, Heng Xu, Yoon-Kyu Song, Barry W Connors, and Arto V Nurmikko. Compact semiconductor light-emitting diodes for dynamic imaging of neuronal circuitry. *IEEE Journal of selected topics in quantum electronics*, 11(4):785–790, 2005.

- [68] Yuejun Chen, Man Xiong, and Su-Chun Zhang. Illuminating parkinson’s therapy with optogenetics. *Nature biotechnology*, 33(2):149, 2015.
- [69] B Zorman, Mushti V Ramakrishna, and RA Friesner. Quantum confinement effects in cdse quantum dots. *The Journal of Physical Chemistry*, 99(19):7649–7653, 1995.
- [70] Louis Brus. Electronic wave functions in semiconductor clusters: experiment and theory. *The Journal of Physical Chemistry*, 90(12):2555–2560, 1986.
- [71] Benjamin S Mashford, Tich-Lam Nguyen, Gerard J Wilson, and Paul Mulvaney. All-inorganic quantum-dot light-emitting devices formed via low-cost, wet-chemical processing. *Journal of Materials Chemistry*, 20(1):167–172, 2010.
- [72] JM Caruge, JE Halpert, V Wood, V Bulović, and MG Bawendi. Colloidal quantum-dot light-emitting diodes with metal-oxide charge transport layers. *Nature photonics*, 2(4):247–250, 2008.
- [73] Yasuhiro Shirasaki, Geoffrey J Supran, Mounqi G Bawendi, and Vladimir Bulović. Emergence of colloidal quantum-dot light-emitting technologies. *Nature Photonics*, 7(1):13–23, 2013.
- [74] Minghui Yang, Alireza Javadi, and Shaoqin Gong. Sensitive electrochemical immunosensor for the detection of cancer biomarker using quantum dot functionalized graphene sheets as labels. *Sensors and Actuators B: Chemical*, 155(1):357–360, 2011.
- [75] Zhexiang Zou, Dan Du, Jun Wang, Jordan N Smith, Charles Timchalk, Yaoqun Li, and Yuehe Lin. Quantum dot-based immunochromatographic fluorescent biosensor for biomonitoring trichloropyridinol, a biomarker of exposure to chlorpyrifos. *Analytical chemistry*, 82(12):5125–5133, 2010.
- [76] Mei Hu, Juan Yan, Yao He, Haoting Lu, Lixing Weng, Shiping Song, Chunhai Fan, and Lianhui Wang. Ultrasensitive, multiplexed detection of cancer biomarkers directly in serum by using a quantum dot-based microfluidic protein chip. *ACS nano*, 4(1):488–494, 2009.

- [77] Fei Zhao, Jing Gao, Long Fang, Xia Yin, Xiaofang Jiang, Yehua Su, Yongyin Kang, and Zhicheng Song. Quantum dots for wide color gamut displays from photoluminescence to electroluminescence. *Nanoscale research letters*, 12(1):154, 2017.
- [78] Dennis EJGJ Dolmans, Dai Fukumura, and Rakesh K Jain. Photodynamic therapy for cancer. *Nature reviews cancer*, 3(5):380, 2003.
- [79] Chia-Yen Hsu, Ching-Wen Chen, Hsiu-Ping Yu, Yan-Fu Lin, and Ping-Shan Lai. Bioluminescence resonance energy transfer using luciferase-immobilized quantum dots for self-illuminated photodynamic therapy. *Biomaterials*, 34(4):1204–1212, 2013.
- [80] Min-Kyung So, Chenjie Xu, Andreas M Loening, Sanjiv S Gambhir, and Jianghong Rao. Self-illuminating quantum dot conjugates for in vivo imaging. *Nature biotechnology*, 24(3):339, 2006.
- [81] Hao Chen, Juan He, Raymond Lanza fame, Istvan Stadler, Hamid El Hamidi, Hui Liu, Jonathan Celli, Michael R Hamblin, Yingying Huang, Emily Oakley, et al. Quantum dot light emitting devices for photomedical applications. *Journal of the Society for Information Display*, 25(3):177–184, 2017.
- [82] Hyunsu Cho, Changhun Yun, Jae-Woo Park, and Seunghyup Yoo. Highly flexible organic light-emitting diodes based on zns/ag/wo 3 multilayer transparent electrodes. *Organic Electronics*, 10(6):1163–1169, 2009.
- [83] James A Schwarz, Cristian I Contescu, and Karol Putyera. *Dekker encyclopedia of nanoscience and nanotechnology*, volume 3. CRC press, 2004.
- [84] Jeffrey B Fortin and Toh-Ming Lu. *Chemical vapor deposition polymerization: the growth and properties of parylene thin films*. Springer Science & Business Media, 2003.
- [85] Bo Lu. *Parylene as a new membrane material for biomems applications*. California Institute of Technology, 2012.
- [86] Youngwan Kim, Christopher Choi, En-Chen Chen, Andy GS Daniel, Amrita Masurkar, Theodore H Schwartz, Hongtao Ma, and Ioannis Kymissis. An ultra thin implantable

- system for cerebral blood volume monitoring using flexible oled and opd. In *Electron Devices Meeting (IEDM), 2015 IEEE International*, pages 29–6. IEEE, 2015.
- [87] Jiangeng Xue, Soichi Uchida, Barry P Rand, and Stephen R Forrest. Asymmetric tandem organic photovoltaic cells with hybrid planar-mixed molecular heterojunctions. *Applied Physics Letters*, 85(23):5757–5759, 2004.
- [88] Kristin L Mutolo, Elizabeth I Mayo, Barry P Rand, Stephen R Forrest, and Mark E Thompson. Enhanced open-circuit voltage in subphthalocyanine/c60 organic photovoltaic cells. *Journal of the American Chemical Society*, 128(25):8108–8109, 2006.
- [89] Samuel P Subbarao, Matthias E Bahlke, and Ioannis Kymissis. Laboratory thin-film encapsulation of air-sensitive organic semiconductor devices. *IEEE Transactions on Electron Devices*, 57(1):153–156, 2010.
- [90] Shyuan Yang, Steve Park, Johannes Bintinger, Yvan Bonnassieux, and Ioannis Kymissis. P-99: Pneumatic nozzle printing as a versatile approach to crystal growth management and patterning of printed organic thin film transistors. In *SID Symposium Digest of Technical Papers*, volume 47, pages 1502–1505. Wiley Online Library, 2016.
- [91] Gunter Hoxter. Suggested isosbestic wavelength calibration in clinical analyses. *Clinical chemistry*, 25(1):143–146, 1979.
- [92] WG Zijlstra, A Buursma, and WP Meeuwse-Van der Roest. Absorption spectra of human fetal and adult oxyhemoglobin, de-oxyhemoglobin, carboxyhemoglobin, and methemoglobin. *Clinical chemistry*, 37(9):1633–1638, 1991.
- [93] Mingrui Zhao, Rose Allea, Hongtao Ma, Andy GS Daniel, and Theodore H Schwartz. Optogenetic tools for modulating and probing the epileptic network. *Epilepsy research*, 116:15–26, 2015.
- [94] Antti Hassinen, Iwan Moreels, Kim De Nolf, Philippe F Smet, Jose A C Martins, and Zeger Hens. Short-chain alcohols strip x-type ligands and quench the luminescence of pbse and cdse quantum dots, acetonitrile does not. *Journal of the American Chemical Society*, 134(51):20705–20712, 2012.



- [95] Byeong Guk Jeong, Young-Shin Park, Jun Hyuk Chang, Ikjun Cho, Jai Kyeong Kim, Heesuk Kim, Kookheon Char, Jinhan Cho, Victor I Klimov, Philip Park, et al. Colloidal spherical quantum wells with near-unity photoluminescence quantum yield and suppressed blinking. *ACS nano*, 10(10):9297–9305, 2016.
- [96] Margaret A Hines and Philippe Guyot-Sionnest. Synthesis and characterization of strongly luminescing zns-capped cdse nanocrystals. *The Journal of Physical Chemistry*, 100(2):468–471, 1996.
- [97] Leslie S Hamachi, Ilan Jen-La Plante, Aidan C Coryell, Jonathan De Roo, and Jonathan S Owen. Kinetic control over cds nanocrystal nucleation using a library of thiocarbonates, thiocarbamates, and thioureas. *Chemistry of Materials*, 29(20):8711–8719, 2017.
- [98] Yuehui Zhou and Michael K Denk. Synthesis and reactivity of subvalent compounds. part 13: Reaction of triethyl orthoformate with amines and selenium—A convenient one-step three-component synthesis for selenoureas. *Tetrahedron letters*, 44(6):1295–1299, 2003.

# Appendix

## Quantum Dot Synthesis

Colloidal quantum dots are typically synthesized by “arrested precipitation”, where a surfactant stabilized solution of semiconductor nanoparticles are capped with organic ligands.[?] The precipitated nanocrystals are purified by filtration or centrifugation and washed. The dry QDs are then re-suspended in a compatible solvent for application by solution processing in optoelectronic devices. Although the organic ligands provide size tunability and solubility, they can also lower the photoluminescent yield of the QDs and are vulnerable to degradation.[94] QDs with an inorganic shell have been shown to improve photoluminescent yield and stability.[95, 96]

The QDs used in this work (Chapter 4), have a CdS/CdSe/CdS core shell structure (Figure 5.1), prepared by first forming CdS and then growing CdSe and outer CdS layers.[95] Zincblende CdS nanocrystals of the appropriate size were synthesized grown using a cadmium oleate solution with a sulphur-based precursor solution, as described in work by Hamachi et al.[97] Without purifying the nanocrystals, the CdSe shell layer is grown using cadmium oleate and either N,N'-diethyl imidazolidine-2-selenone or N,N'-di tert-butyl imidazolidine-2-selenone as selenide precursors.[98] The outer CdS shell is grown with slight modifications[95] at either 240°C or 290°C using cadmium oleate and another sulfide precursor. The nanocrystals are purified by centrifugation and resuspended in anhydrous toluene. The synthesis process and storage occurs in an airfree glovebox prior to use. The resulting absorption spectra and photoluminescent spectra of the QDs suspended in toluene are shown in Figure 5.2.

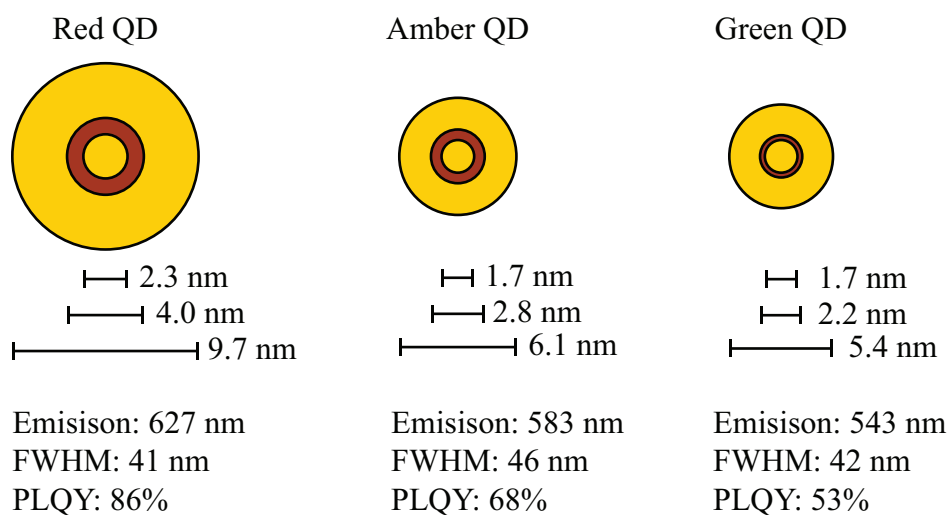


Figure 5.1: Diagram of 3 variants of CdS/CdSe/CdS core shell quantum dots.

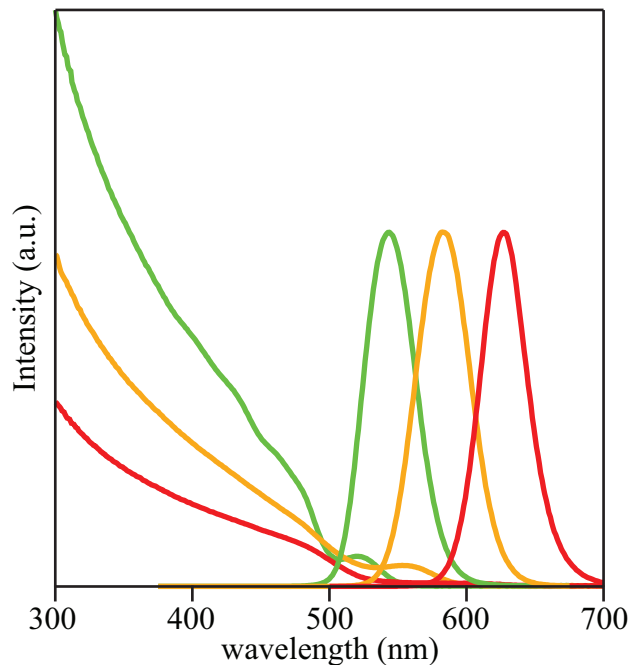


Figure 5.2: QD absorption (left) and photoluminescent (right) spectra for 3 different variants of CdS/CdSe/CdS core shell QDs suspended in toluene.